

Nitrogen Abundance Distribution in the Inner Milky Way

JORGE L. PINEDA,¹ SHINJI HORIUCHI,² L. D. ANDERSON,^{3,4,5} MATTEO LUISI,^{6,4} WILLIAM D. LANGER,¹ PAUL F. GOLDSMITH,¹
THOMAS B. H. KUIPER,¹ CHRISTIAN FISCHER,⁷ YAN GONG,⁸ ANDREAS BRUNTHALER,⁸ MICHAEL RUGEL,^{9,10,8,*} AND
KARL M. MENTEN⁸

¹Jet Propulsion Laboratory, California Institute of Technology, 4800 Oak Grove Drive, Pasadena, CA 91109-8099, USA

²CSIRO Space & Astronomy/NASA Canberra Deep Space Communication Complex, PO Box 1035, Tuggeranong ACT 2901, Australia

³Department of Physics and Astronomy, West Virginia University, Morgantown, WV 26506, USA

⁴Center for Gravitational Waves and Cosmology, West Virginia University, Chestnut Ridge Research Building, Morgantown, WV 26505, USA

⁵Green Bank Observatory, P.O. Box 2, Green Bank, WV 24944, USA

⁶Department of Physics, Westminister College, New Wilmington, PA 16172, USA

⁷Deutsches SOFIA Institut, Pfaffenwaldring 29, 70569 Stuttgart, Germany

⁸Max-Planck-Institut für Radioastronomie, Auf dem Hügel 69, 53121 Bonn, Germany

⁹Center for Astrophysics, Harvard & Smithsonian, 60 Garden St., Cambridge, MA 02138, USA

¹⁰National Radio Astronomy Observatory, 1003 Lopezville Rd, Socorro, NM 87801, USA

Submitted to ApJ

ABSTRACT

We combine a new Galactic plane survey of Hydrogen Radio Recombination Lines (RRLs) with far-infrared (FIR) surveys of ionized Nitrogen, N⁺, to determine Nitrogen abundance across Galactic radius. RRLs were observed with NASA DSS-43 70m antenna and the Green Bank Telescope in 108 lines-of-sight spanning $-135^\circ < l < 60^\circ$, at $b = 0^\circ$. These positions were also observed in [N II] 122 μ m and 205 μ m lines with the *Herschel Space Observatory*. Combining RRL and [N II] 122 μ m and 205 μ m observations in 41 of 108 samples with high signal-to-noise ratio, we studied ionized Nitrogen abundance distribution across Galactocentric distances of 0–8 kpc. Combined with existing Solar neighborhood and Outer galaxy N/H abundance determinations, we studied this quantity’s distribution within the Milky Way’s inner 17 kpc for the first time. We found a Nitrogen abundance gradient extending from Galactocentric radii of 4–17 kpc in the Galactic plane, while within 0–4 kpc, the N/H distribution remained flat. The gradient observed at large Galactocentric distances supports inside-out galaxy growth with the additional steepening resulting from variable star formation efficiency and/or radial flows in the Galactic disk, while the inner 4 kpc flattening, coinciding with the Galactic bar’s onset, may be linked to radial flows induced by the bar potential. Using SOFIA/FIFI-LS and *Herschel*/PACS, we observed the [N III] 57 μ m line to trace doubly ionized gas contribution in a sub-sample of sightlines. We found negligible N⁺⁺ contributions along these sightlines, suggesting mostly singly ionized Nitrogen originating from low ionization H II region outskirts.

Keywords: ISM: molecules — ISM: structure

1. INTRODUCTION

The regulation of star formation in galaxies is a key driver of galaxy evolution. As galaxies evolve, gas from the circum-galactic medium accretes into their disks, cooling down and forming dense molecular clouds where star formation takes place. As massive stars form, their radiative and mechanical feedback ionizes and disperses their surrounding

gas slowing the gravitational collapse and star formation. Stellar feedback can also result in large scale outflows of gas that is transported back to the circum-galactic medium which, depending on how the energy and momentum from stellar feedback couples with the gas, can either accrete back into the disk of the galaxy, restarting the whole process, or be expelled to the inter-galactic medium. The interplay between accretion and outflows of gas into and out of the disk of galaxies, molecular cloud formation, and the effects of stellar feedback into the interstellar medium determines the efficiency and rate at which gas is converted into stars in galaxies. Therefore understanding these processes individ-

Corresponding author: Jorge L. Pineda

Jorge.Pineda@jpl.nasa.gov

* M.R.R. is a Jansky Fellow of the National Radio Astronomy Observatory, USA

ually as well as their interplay is key for understanding the regulation of star formation and the evolution of galaxies.

The distribution of elemental abundances in the disk of galaxies provides a fundamental observational constraint for models of the formation and evolution of galaxies. Elements such as C, N, and O, are products of “primary” and “secondary” processes in massive and inter-mediate mass stars (Johnson 2019) and therefore their abundances are related to the type of stars, star formation rate, and star formation history at a given location, with each element having a different enrichment timescale. Metallicities are typically referred in terms of the Oxygen abundance with respect to hydrogen, O/H. However the abundance of elements such as Nitrogen and Carbon can also provide important insights on the chemical evolution of galaxies. Oxygen is mostly formed in massive stars and its production timescale is short (~ 0.1 Gyr; e.g. Maiolino & Mannucci 2019). Carbon and Nitrogen however, can also be produced in intermediate mass stars, and the timescales for their production are much longer than those for Oxygen (1–10 Gyr). Therefore, Nitrogen and/or Carbon abundances, alongside that of Oxygen, can provide important information on the star formation history in galaxies.

The distribution of elements in the disk of galaxies provides important constraints on the growth of galaxies as it is related to the radial gas accretion profile in galaxies, which is an important parameter on galaxy chemical evolution models (Larson 1976; Matteucci & Francois 1989; Boissier & Prantzos 1999; Pezzulli & Fraternali 2016). Several studies of the distribution of elemental abundances in the disk of galaxies have been conducted using optical lines (Sánchez et al. 2014; Pérez-Montero et al. 2016; Sánchez-Menguiano et al. 2016; Belfiore et al. 2017). Belfiore et al. (2017) studied a large sample of galaxies, finding that the abundance of Oxygen relative to that of Hydrogen, O/H, decreases with galactocentric distance with a slope that steepens with the galaxy’s stellar mass. For galaxies at the high end of the stellar mass range in their sample ($M > 10^{10.5} M_{\odot}$), a flattening of the O/H distribution is observed. They also studied the Nitrogen abundance relative to that of Oxygen and found that the N/O ratio increases with galactocentric distance and does not flatten in the inner parts of massive galaxies. These observations are interpreted in the context of inside–out growth of galaxy disks in which the central parts of massive galaxies reach a metallicity equilibrium, in which metal production is balanced by metal consumption by star formation expulsion by outflows, and while the outer part continues accreting less enriched gas. Note however that, in the central parts of massive galaxies, the dust extinction becomes significant and therefore enriched gas close to the galaxy’s center might be unaccounted for by optical and near–IR observations (Puglisi et al. 2017; Calabrò et al. 2018).

It is important to test whether the properties of abundance distributions observed in nearby galaxies also apply to the Milky Way. Detailed studies of the properties of the interstellar medium and star formation at high spatial resolution are currently only possible in the Milky Way. Therefore, by studying the elemental abundance distribution in the Milky

Way, we can obtain a deeper insight into the nature of these distributions, which in turn can be used to interpret the results obtained over large samples of unresolved, external galaxies. The abundance distributions in the Milky Way have been traditionally obtained observing H II regions with optical lines in a variety of environments. These observations which are mostly focused on nearby H II regions, where dust extinction obscures these optical lines moderately, have been used to infer that the abundance of Oxygen and Nitrogen increase with Galactocentric distance from the outer galaxy inward to $R_{\text{gal}} = 4$ kpc (Esteban & García-Rojas 2018; Arellano-Córdova et al. 2021, see also Romano 2022 and references therein). Due to increased dust extinction, optical studies are however unable to probe the inner Galaxy, where most of the star formation takes place, and which is thought to have formed during the early stages of the Milky Way’s evolution. Therefore, these observations have been unable to test the flattening in the O/H distribution and a possible increase of the N/O ratio observed in the central parts of external galaxies with similar stellar masses as the Milky Way’s.

Longer wavelength observations, including those of far-infrared fine structure lines, radio continuum, and hydrogen radio recombination lines can be combined to determine the abundance of elements with the advantage that they are unobscured by dust, enabling elemental abundance determination deep into the inner galaxy (Simpson et al. 1995; Afflerbach et al. 1997; Rudolph et al. 1997; Simpson et al. 2004; Rudolph et al. 2006; Balser et al. 2011). These observations however are limited to small samples mostly focused in dense (ultra–)compact H II regions that might have complex ionization structures, and thus require a large number of spectral line observations to determine elemental abundances. Goldsmith et al. (2015) presented a survey of 149 lines–of–sight observed uniformly in the Galactic plane in the [N II] 205 μm and 122 μm lines at $b = 0^{\circ}$ using the *Herschel*/PACS instrument. The [N II] 122 μm /205 μm ratio provides an accurate determination of the electron density that is independent of Nitrogen abundance and has a weak dependence on electron temperature. The electron densities derived in their sample show little scatter with a mean value of about 30 cm^{-3} , suggesting that these observations are tracing an extended moderate density ionized gas component in the ISM which is likely to have moderate far–UV (FUV) and extreme–UV (EUV) fields, and thus the ionization structure is simpler than in compact H II regions. In Pineda et al. (2019) we derived Nitrogen abundances in a sample of 10 sight lines taken from the Goldsmith et al. (2015) survey by combining [N II] and RRL observations. We found that the distribution of Nitrogen abundances in the inner Galaxy derived from our data has a linear slope that is consistent with that found in the outer Galaxy in optical studies. In this paper we present an analysis of a larger sample to confirm these results and investigate the distribution of Nitrogen in the inner Galactic plane.

We present in this paper a Galactic plane survey of Hydrogen Recombination Lines, covering the range between $-135^{\circ} < l < 60^{\circ}$ and $b = 0^{\circ}$ using the NASA Deep Space Network Station 43 (DSS–43) in Canberra, Australia,

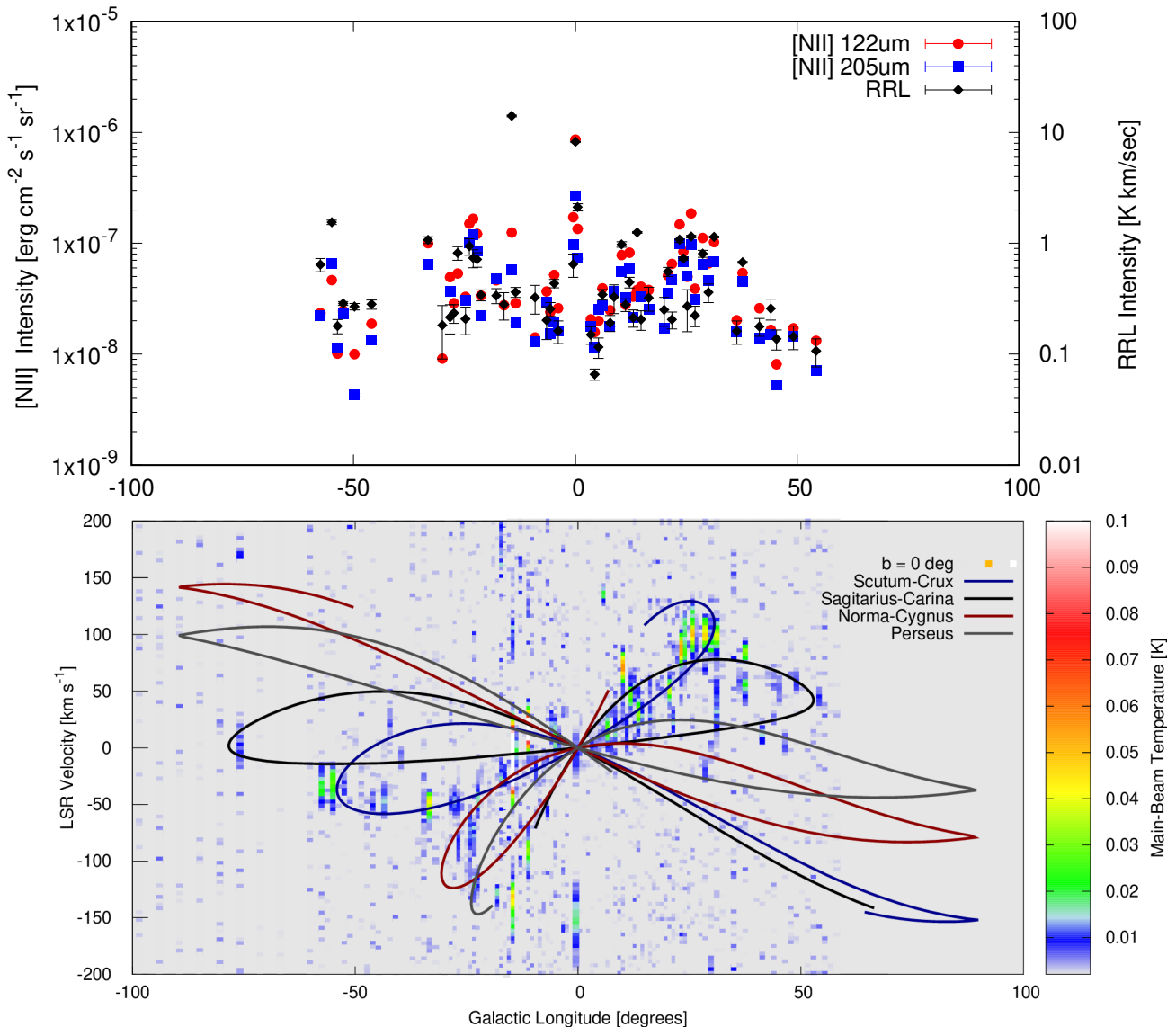


Figure 1. (*upper panel*) Distribution of the [N II] 122 μm , 205 μm , and RRL emission as a function of Galactic longitude. (*lower panel*) Position velocity map of Hydrogen recombination line emission for the observed GOT C+ LOS between $l = -100^\circ$ and 100° at $b = 0^\circ$. The position-velocity map is overlaid with projections of the Scutum-Crux, Sagittarius-Carina, Perseus, and Norma-Cygnus Milky Way spiral arms.

and the Green Bank telescope. The lines-of-sight coincide with those observed by *Herschel*/HIFI in [C II] (Langer et al. 2010; Pineda et al. 2013) and by *Herschel*/PACS in [N II] 122 μm and 205 μm (Goldsmith et al. 2015). The high-velocity resolution observations of RRLs will allow us to disentangle the source of [N II] emission in the Galactic plane. In this paper we focus on combining the RRL data set with that observed in [N II] with *Herschel* to derive the abundance of ionized Nitrogen with respect to ionized Hydrogen in the inner parts of the Milky Way. This data set will be also combined with SOFIA/FIFI-LS and *Herschel* observations of the [N III] 57 μm to account for the contribution of higher ionization states of Nitrogen, such as N^{++} .

The paper is organized as follows. In Section 2 we describe the RRL, [N II], and [N III] 57 μm observations. In

Section 3, we describe our method to determine the Nitrogen abundance from our observations and we discuss the properties of the derived Nitrogen abundance distribution. We also discuss the implications of the observed distribution in terms of theoretical predictions from chemical evolution models. In Section 4 we summarize our results.

2. OBSERVATIONS

We surveyed the Galactic plane in the Hydrogen radio recombination line (RRL) emission, using RRL transitions between $\text{H}89\alpha$ and $\text{H}92\alpha$, covering 108 lines-of-sight (LOS) in the $-135^\circ < l < -60^\circ$ range in Galactic longitude and at a Galactic latitude of $b = 0^\circ$, with the NASA DSN DSS-43 70m telescope and the Green Bank Telescope. These LOS correspond to a subsample of the *Herschel* Open Time Key

Table 1. [N II], [N III], RRL, and radio continuum intensities for $l \geq 0^\circ$.

LOS	l	b	[N II] 122 μ m [$\times 10^{-8}$] [W m $^{-2}$ sr $^{-1}$]	[N II] 205 μ m [$\times 10^{-8}$] [W m $^{-2}$ sr $^{-1}$]	[N III] 57 μ m [$\times 10^{-7}$] [W m $^{-2}$ sr $^{-1}$]	RRL [K km s $^{-1}$]	RRL I.D.	<T _C > free-free at 8.5GHz [K]
G000.0+0.0	0.000	0.0	86.165 ± 0.097	26.426 ± 0.089	4.61 ± 0.76	8.23 ± 0.08	H89 α	6.97 ± 0.01
G000.5+0.0	0.500	0.0	13.509 ± 0.025	7.296 ± 0.068	–	2.12 ± 0.16	H89 α	2.17 ± 0.01
G003.5+0.0	3.478	0.0	2.064 ± 0.005	1.775 ± 0.019	–	0.15 ± 0.03	H89 α	0.06 ± 0.01
G004.3+0.0	4.348	0.0	1.580 ± 0.003	1.149 ± 0.021	–	0.09 ± 0.04	H89 α	0.05 ± 0.01
G005.2+0.0	5.217	0.0	1.999 ± 0.012	2.566 ± 0.063	–	0.12 ± 0.02	H89 α	0.07 ± 0.01
G006.1+0.0	6.087	0.0	3.927 ± 0.006	2.749 ± 0.014	–	0.35 ± 0.04	H89 α	0.19 ± 0.01
G007.8+0.0	7.826	0.0	2.486 ± 0.004	1.780 ± 0.018	–	0.19 ± 0.03	H89 α	0.15 ± 0.01
G008.7+0.0	8.696	0.0	3.689 ± 0.012	3.707 ± 0.083	–	0.33 ± 0.10	H89 α	0.34 ± 0.02
G010.4+0.0	10.435	0.0	7.827 ± 0.017	5.505 ± 0.072	3.61 ± 0.40	0.98 ± 0.06	H89 α	0.43 ± 0.02
G011.3+0.0	11.304	0.0	2.798 ± 0.013	3.232 ± 0.097	–	0.28 ± 0.04	H89 α	0.09 ± 0.01
G012.2+0.0	12.174	0.0	8.228 ± 0.017	5.864 ± 0.067	<2.62 ± 0.87	0.45 ± 0.05	H89 α	0.18 ± 0.01
G013.0+0.0	13.043	0.0	3.306 ± 0.006	2.161 ± 0.019	–	0.35 ± 0.05	H89 α	0.20 ± 0.01
G013.9+0.0	13.913	0.0	4.981 ± 0.013	3.793 ± 0.078	–	1.26 ± 0.02	H89 α	0.29 ± 0.02
G014.8+0.0	14.783	0.0	4.055 ± 0.012	3.300 ± 0.059	–	0.21 ± 0.04	H89 α	0.16 ± 0.01
G016.5+0.0	16.522	0.0	3.791 ± 0.005	2.537 ± 0.009	–	0.32 ± 0.08	H89 α	0.13 ± 0.01
G020.0+0.0	20.000	0.0	1.715 ± 0.004	1.717 ± 0.011	–	0.25 ± 0.07	H89 α	0.12 ± 0.01
G020.9+0.0	20.870	0.0	5.122 ± 0.012	3.570 ± 0.060	–	0.56 ± 0.05	H89 α	0.25 ± 0.01
G021.7+0.0	21.739	0.0	6.533 ± 0.015	4.723 ± 0.064	–	0.22 ± 0.04	H89 α	0.22 ± 0.01
G023.5+0.0	23.478	0.0	14.796 ± 0.016	9.960 ± 0.061	<2.42 ± 0.81	1.08 ± 0.06	H89 α	0.46 ± 0.01
G024.3+0.0	24.348	0.0	8.428 ± 0.019	6.898 ± 0.063	3.67 ± 0.50	0.73 ± 0.03	H89 α	0.30 ± 0.01
G025.2+0.0	25.217	0.0	4.991 ± 0.014	5.093 ± 0.061	–	0.27 ± 0.11	H89 α	0.19 ± 0.01
G026.1+0.0	26.087	0.0	18.625 ± 0.021	9.721 ± 0.075	<4.64 ± 1.55	1.15 ± 0.03	H89 α	0.45 ± 0.01
G027.0+0.0	26.956	0.0	3.898 ± 0.006	3.141 ± 0.020	–	0.22 ± 0.05	H89 α	0.17 ± 0.01
G028.7+0.0	28.696	0.0	11.173 ± 0.013	6.507 ± 0.065	2.64 ± 0.28	0.81 ± 0.06	H89 α	0.52 ± 0.02
G030.0+0.0	30.000	0.0	6.596 ± 0.013	4.577 ± 0.075	–	0.38 ± 0.07	H89 α	0.40 ± 0.02
G031.3+0.0	31.277	0.0	10.271 ± 0.015	6.857 ± 0.068	–	1.14 ± 0.02	H89 α	0.45 ± 0.01
G036.4+0.0	36.383	0.0	2.020 ± 0.011	1.602 ± 0.075	–	0.16 ± 0.04	H89 α	0.09 ± 0.01
G037.7+0.0	37.660	0.0	5.400 ± 0.010	4.505 ± 0.073	–	0.67 ± 0.01	H89 α	0.25 ± 0.01
G041.5+0.0	41.489	0.0	2.600 ± 0.003	1.387 ± 0.010	–	0.19 ± 0.03	H89 α	0.15 ± 0.01
G044.0+0.0	44.043	0.0	1.658 ± 0.002	1.501 ± 0.020	–	0.26 ± 0.06	H89 α	0.08 ± 0.01
G045.3+0.0	45.319	0.0	0.812 ± 0.002	0.525 ± 0.012	–	0.14 ± 0.03	H89 α	0.07 ± 0.01
G049.1+0.0	49.149	0.0	1.716 ± 0.012	1.447 ± 0.055	–	0.14 ± 0.03	H89 α	0.15 ± 0.01
G054.3+0.0	54.255	0.0	1.322 ± 0.003	0.716 ± 0.011	–	0.11 ± 0.03	H89 α	0.09 ± 0.01

project, GOTC+ (Langer et al. 2010; Pineda et al. 2013), which observed the [C II] 158 μ m line at high spectral resolution with the HIFI instrument. The GOTC+ sample with $b = 0^\circ$ was also observed in [N II] 122 μ m and 205 μ m by Goldsmith et al. (2015). The LOS are sampled every $\sim 1^\circ$ in the inner galaxy ($|l| < 60^\circ$) and every $\sim 2^\circ$ – 5° in the outer galaxy. The GOTC+ goal of adopting this sampling of the Galactic plane was to obtain a statistical sample of a large number of environments distributed across the Galaxy.

In the upper panel of Figure 1 we show the [N II] 205 μ m, 122 μ m, and RRL integrated intensities as a function of Galactic longitude. These intensities are listed in Tables 1 and 2. The lower panel of Figure 1 shows the longitude–velocity distribution of the observed RRL emission. The

longitude–velocity (LV) map is overlaid with projections of the Scutum–Crux, Sagittarius–Carina, Perseus, and Norma–Cygnus Milky Way spiral arms. For the LV map we used the fits to the parameters determining the logarithmic spiral arms presented by Steiman–Cameron et al. (2010). We assumed a flat rotation curve with parameters presented by Reid et al. (2014, see Section 3.1.3). We see a good correspondence between RRL emission and spiral arms, with an enhanced RRL emission at the spiral arm tangents, which can be explained by the longer path length for a given velocity range in these regions.

In Figure 2 we show the [N II] 122 μ m and 205 μ m intensities as a function of the RRL integrated intensity for our sample. The figure shows a linear correlation that suggests

Table 2. [N II], [N III], RRL, and radio continuum intensities for $l < 0^\circ$.

LOS	l	b	[N II] 122 μ m [$\times 10^{-8}$] [W m $^{-2}$ sr $^{-1}$]	[N II] 205 μ m [$\times 10^{-8}$] [W m $^{-2}$ sr $^{-1}$]	[N III] 57 μ m [$\times 10^{-7}$] [W m $^{-2}$ sr $^{-1}$]	RRL [K km s $^{-1}$]	RRL I.D.	<T _C > free-free at 8.5GHz [K]
G302.6+0.0	302.553	0.0	2.352 \pm 0.003	2.225 \pm 0.016	–	0.64 \pm 0.09	H91 α	0.16 \pm 0.00
G305.1+0.0	305.106	0.0	4.656 \pm 0.009	6.512 \pm 0.070	–	1.55 \pm 0.07	H91 α	0.44 \pm 0.00
G306.4+0.0	306.383	0.0	1.012 \pm 0.003	1.134 \pm 0.018	–	0.18 \pm 0.03	H92 α	0.10 \pm 0.00
G307.7+0.0	307.660	0.0	2.467 \pm 0.012	2.312 \pm 0.067	–	0.29 \pm 0.01	H92 α	0.17 \pm 0.00
G310.2+0.0	310.213	0.0	0.999 \pm 0.003	0.429 \pm 0.011	–	0.27 \pm 0.02	H92 α	0.15 \pm 0.00
G314.0+0.0	314.043	0.0	1.885 \pm 0.004	1.336 \pm 0.010	–	0.28 \pm 0.03	H92 α	0.16 \pm 0.00
G316.6+0.0	316.596	0.0	5.633 \pm 0.014	4.563 \pm 0.073	–	0.63 \pm 0.03	H92 α	0.38 \pm 0.00
G317.9+0.0	317.872	0.0	4.064 \pm 0.013	3.000 \pm 0.060	–	0.60 \pm 0.03	H92 α	0.37 \pm 0.00
G326.8+0.0	326.808	0.0	10.015 \pm 0.015	6.501 \pm 0.067	–	1.07 \pm 0.07	H91 α	0.36 \pm 0.00
G330.0+0.0	330.000	0.0	1.470 \pm 0.004	0.914 \pm 0.014	–	0.18 \pm 0.09	H91 α	0.18 \pm 0.01
G331.7+0.0	331.739	0.0	4.953 \pm 0.014	3.708 \pm 0.071	–	0.22 \pm 0.06	H91 α	0.27 \pm 0.02
G332.6+0.0	332.609	0.0	4.583 \pm 0.013	2.878 \pm 0.068	–	1.17 \pm 0.17	H92 α	0.28 \pm 0.02
G333.5+0.0	333.478	0.0	9.275 \pm 0.011	5.345 \pm 0.057	–	0.82 \pm 0.12	H91 α	0.43 \pm 0.02
G336.1+0.0	336.087	0.0	15.073 \pm 0.022	10.208 \pm 0.061	–	0.94 \pm 0.16	H91 α	0.53 \pm 0.03
G337.0+0.0	336.957	0.0	16.668 \pm 0.022	11.856 \pm 0.072	–	0.92 \pm 0.13	H91 α	1.08 \pm 0.07
G337.8+0.0	337.826	0.0	12.177 \pm 0.014	8.488 \pm 0.071	–	0.72 \pm 0.11	H91 α	0.57 \pm 0.04
G338.7+0.0	338.696	0.0	3.371 \pm 0.005	2.202 \pm 0.014	–	0.60 \pm 0.09	H92 α	0.24 \pm 0.02
G342.2+0.0	342.174	0.0	4.645 \pm 0.014	4.807 \pm 0.065	–	0.53 \pm 0.08	H91 α	0.29 \pm 0.02
G343.9+0.0	343.913	0.0	3.718 \pm 0.013	2.761 \pm 0.064	–	0.28 \pm 0.08	H91 α	0.24 \pm 0.02
G345.7+0.0	345.652	0.0	12.527 \pm 0.015	5.812 \pm 0.074	–	14.12 \pm 0.28	H89 α	1.73 \pm 0.07
G346.5+0.0	346.522	0.0	2.879 \pm 0.011	1.899 \pm 0.060	–	0.45 \pm 0.08	H89 α	0.29 \pm 0.02
G349.1+0.0	349.130	0.0	21.023 \pm 0.025	9.128 \pm 0.061	–	3.92 \pm 0.05	H89 α	1.51 \pm 0.06
G350.9+0.0	350.870	0.0	1.410 \pm 0.011	1.302 \pm 0.060	–	0.33 \pm 0.09	H89 α	0.14 \pm 0.01
G353.5+0.0	353.478	0.0	3.672 \pm 0.006	2.945 \pm 0.014	–	0.20 \pm 0.07	H89 α	0.21 \pm 0.02
G354.3+0.0	354.348	0.0	2.396 \pm 0.012	1.534 \pm 0.066	–	0.26 \pm 0.04	H89 α	0.16 \pm 0.01
G355.2+0.0	355.217	0.0	5.180 \pm 0.012	1.953 \pm 0.051	–	0.49 \pm 0.04	H89 α	0.46 \pm 0.06
G356.1+0.0	356.087	0.0	2.596 \pm 0.004	1.628 \pm 0.008	–	0.16 \pm 0.04	H89 α	0.13 \pm 0.02
G359.5+0.0	359.500	0.0	17.209 \pm 0.027	9.763 \pm 0.091	–	0.68 \pm 0.15	H89 α	1.06 \pm 0.01

that both [N II] and RRL line emission are tracing the same ionized gas, and that Nitrogen is mostly in a singly ionized form in our sample, even in the conditions of the Galactic center, whose data points in the top right of Figure 2. A more detailed discussion about the ionization of Nitrogen is presented in Section 3.1.2).

2.1. Hydrogen Recombination Line Observations

We used the NASA DSN DSS–43 telescope in Camberra, Australia, to observe 45 LOS in our sample, covering the southern sky portion of the Galactic plane. We used X–band receiver in position–switching mode to observe the H91 α and H92 α hydrogen radio recombination lines at 8.58482 GHz and 8.30938 GHz, respectively. The angular resolution of the DSS–43 at 8.420 GHz is 115". We converted the data from an antenna temperature to a main beam temperature scale us-

ing a main beam efficiency of 0.78¹. Both lines were re-sampled to a common spectral grid and averaged together to increase the signal–to–noise ratio, with the H92 α intensities scaled to correspond to that of the H91 α lines². We fitted a 3rd order polynomial baseline to our data. The resulting spectra have a typical rms noise of 4 mK in a 1 km s $^{-1}$ channel. We also re-observed a subsample of LOS in the

¹ Details in the determination of the aperture efficiency and beamsize of the DSS–43 antenna is available on–line at <https://deepspace.jpl.nasa.gov/dsndocs/810-005/>.

² As seen in Equation (3), in LTE, the intensity of a RRL is proportional to the EM , the line width, and line frequency. Given that EM and Δv are intrinsic properties of the source, the intensity of two RRLs are related by the inverse of the ratio of their frequencies (Balser 2006). In the case when LTE does not apply (Equation 7), however, a dependence on electron density and temperature is introduced to the relationship between two line intensities. For lines with similar principal quantum number, n , this effect is negligible, and assuming LTE is appropriate. For larger Δn , however, NLTE effects need to be taken into account when scaling RRL intensities.

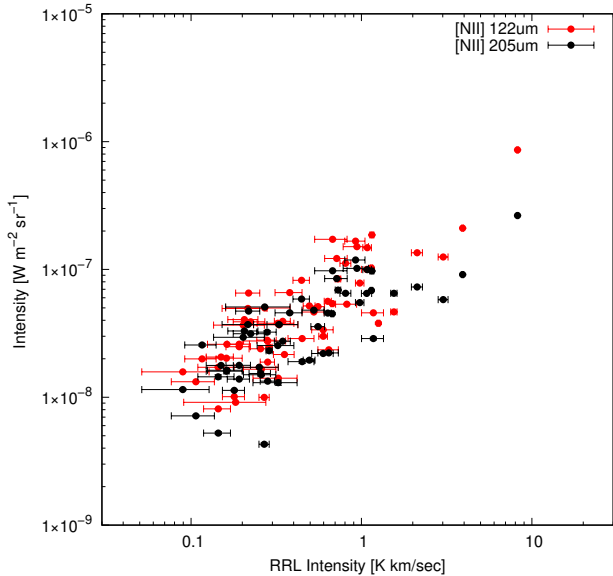


Figure 2. [N II] 122 μm and 205 μm intensities as a function of the RRL integrated intensity.

H89 α (9.17332 GHz) line with the DSS-43 antenna to improve the signal-to-noise using the ROACH2 spectrometer (Virkler et al. 2020). The spectra have a rms noise of 1 mK over a 3 km s $^{-1}$ channel.

We also observed X-band RRLs in 79 LOS in our sample, covering the northern sky portion of the Galactic plane, using the Versatile GBT Astronomical Spectrometer (VEGAS) on the Green Bank Telescope (GBT) in the position-switching mode. The angular resolution of the GBT in X-band is 84 $''$. For each observed direction, we simultaneously measured seven Hn α RRL transitions in the 9 GHz band, H87 α to H93 α , using the techniques discussed in Bania et al. (2010), Anderson et al. (2011), and Balsler et al. (2011), and averaged all spectra together to increase the signal-to-noise ratio using TMBIDL (Bania et al. 2016). The data were resampled to a common grid, intensities scaled to correspond to that for the H89 α line (9.17332 GHz), and we averaged all lines in the band (2 polarizations per transition) together to increase the signal-to-noise ratio. The GBT data was calibrated using a noise diode of known power. The spectra were later corrected with a 3rd order polynomial baseline and smoothed to ~ 1.9 km s $^{-1}$. We converted the intensities from an antenna temperature to main beam temperature using a main beam efficiency of 0.94. The typical rms noise of these data is 2.5 mK in a 1.9 km s $^{-1}$ channel.

2.2. [N II] 122 μm and 205 μm observations

We used *Herschel*/PACS data of the [N II] 205 μm and 122 μm lines that were surveyed by Goldsmith et al. (2015) in 149 GOT C+ LOS with $b = 0^\circ$. We refer to Goldsmith et al. (2015) for the details on the reduction of this data set. The PACS instrument has a 5 \times 5 pixel grid, with a pixel separation of $\sim 9.4''$ corresponding to a footprint of 47 $''$ in the sky. The PACS spectrometer has a resolving power of 1000

at 122 μm and 2000 at 205 μm , corresponding to a velocity resolution of 300 km s $^{-1}$ and 150 km s $^{-1}$, respectively, and therefore the emission lines are spectrally unresolved. The *Herschel* telescope with PACS has a FWHM beam width of 10 $''$ at 122 μm and 15 $''$ at 205 μm .

To improve the signal-to-noise of the observations, and to reduce the contrast between the angular resolution of the [N II] and RRL data sets, we used the footprint-averaged spectra, corresponding to an angular resolution of 47 $''$. (A discussion about beam dilution effects is presented in Section 3.1.1.) Note that there is a slight difference between the [N II] 122 μm and 205 μm intensities we calculated and those presented by Goldsmith et al. (2015), as the latter used a simple average of all pixels in the PACS footprint, while we used a Gaussian-weighted average based on the distance of each pixel to the center of the footprint. The difference between these two approaches is minimal and does not significantly affect the derived electron densities and N $^+$ column densities. The typical rms noise of the observations are $\sim 2 \times 10^{-7}$ erg cm $^{-2}$ s $^{-1}$ sr $^{-1}$ for the 122 μm line and $\sim 6 \times 10^{-7}$ erg cm $^{-2}$ s $^{-1}$ sr $^{-1}$ for the 205 μm line.

2.3. [N III] 57 μm observations

To study the ionization structure of Nitrogen, and to estimate the contribution of highly ionized states of Nitrogen to the total Nitrogen abundance, we observed a subsample of 8 LOS in the [N III] 57 μm line with the Far Infrared Field-Imaging Line Spectrometer (FIFI-LS; Fischer et al. 2018) which is an integral field far-infrared spectrometer on SOFIA. These observations were taken as part of the SOFIA ID 08_0023 and 09_0150 projects.

The [N III] 57 μm spectra were obtained with pointed observations of the FIFI-LS 5 \times 5 pixel footprint in the blue channel (μm), with an angular resolution of 6 $''$ at 57 μm . To improve the signal-to-noise ratio we averaged the spectra in each footprint, and therefore the angular resolution of the average corresponds to the 30 $''$ size of the FIFI-LS footprint. The spectral resolution of FIFI-LS at 57 μm is 280 km s $^{-1}$. Given that the typical line width of the RRL emission in our sample is 25 km s $^{-1}$, the lines observed with FIFI-LS are spectrally unresolved.

We computed the footprint-averaged spectrum for each LOS using the SOSPEX software (Fadda & Chambers 2018) and imported the resulting spectra into GILDAS/CLASS for baseline corrections and fitting. The averaged FIFI-LS spectra at 57 μm shows a steep baseline that results from the effects of rapidly changing atmosphere conditions during flight. The shape of this baseline is similar to that seen for the transmission curve of the atmosphere. We fitted a 3rd order polynomial to the flux spectrum, using our knowledge of the location of the spectral lines from the spectrally resolved RRL spectra to define a window in the flux spectrum where the channels are excluded from the fit. The typical rms noise of the observations is 6.51×10^{-5} erg s $^{-1}$ cm $^{-2}$ sr. We detected the [N III] 57 μm line in 4 out of the 10 LOS. For the undetected LOS, we will use their 3 σ upper limits to con-

strain the contribution from doubly ionized Nitrogen in these locations.

We complemented our analysis with *Herschel*/PACS observations of the [N III] $57\mu\text{m}$, [N II] $122\mu\text{m}$, and [O III] $88\mu\text{m}$ and $52\mu\text{m}$, and SPIRE-FTS [N II] $205\mu\text{m}$ emission observed in the Sagittarius A region in the Galactic center. These observations were presented by, and the data reduction is described in, Goicoechea et al. (2013). In our analysis we used the PACS footprint averaged spectrum and therefore its angular resolution is $\sim 47''$. The SPIRE-FTS [N II] $205\mu\text{m}$ spectrum presented by Goicoechea et al. (2013) was computed in a $30''$ aperture. As with the FIFI-LS observations, the spectral lines observed with *Herschel*/PACS and SPIRE are unresolved in velocity. In Figure 3 we show the detected SOFIA FIFI-LS [N III] $57\mu\text{m}$ spectra. The intensities of the [N III] $57\mu\text{m}$, and 3σ upper limits, are listed in Table 1. We present an analysis of this data set in Section 3.1.2.

2.4. Sample Location with Respect to Known H II Regions

To evaluate potential sources of uncertainties in the derived Nitrogen abundances, such as the presence of doubly ionized Nitrogen and beam dilution effects related to the use of observations from different telescopes in compact sources, we need to understand the nature of the regions we are sampling. As discussed in Section 2, the sample of LOS used in our study is drawn from the *Herschel* GOT C+ survey which provided a uniform sampling of the Galactic plane and therefore it did not intentionally targeted to the center of any specific H II region. Goldsmith et al. (2015) derived electron densities in this sample showing typical values of about 30 cm^{-3} which are higher than what is expected for the Warm Ionized Medium (WIM) but lower than that of compact H II regions. This result suggests that the [N II] emission detected in the GOT C+ sample arises from an extended component of the ionized ISM, which is not closely associated with massive stars.

To further assess the nature of the sources in our sample we studied the environment traced by our sample LOS by searching for the nearest known H II regions from the Wide-field Infrared Survey Explorer (WISE) Catalog of Galactic H II Regions (Anderson et al. 2014). These regions were followed up with RRL and radio continuum observations to confirm that the mid-infrared warm dust emission is associated with ionized gas (Bania et al. 2010; Anderson et al. 2011; Wenger et al. 2019). In Tables 3 and 4, we list the nearest WISE H II region to each LOS in our sample, the distance between the center of the observations' beam and that of the nearest H II region, the radius of the nearest H II region, and the percentage of the RRL beam area that overlaps with the H I region. The radius of a WISE H II region is defined by that of a circular aperture that encloses its associated mid-infrared emission. We find that the majority of LOS in our sample (40 out of 61) do not overlap with known H I regions. There are, however, 12 LOS in which the RRL beam has an overlap with the nearest H II region of over 50%, of which 7 have a 100% overlap.

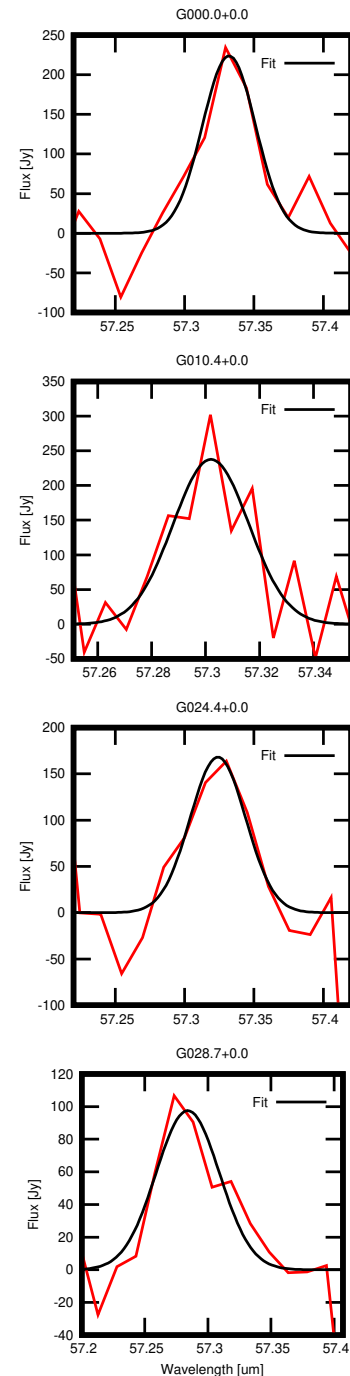


Figure 3. Spectra of the detected [N III] $57\mu\text{m}$ line observed with the FIFI-LS instrument on SOFIA. We also show the Gaussian fit to the data.

We compared the average electron temperatures, volumes densities, and ionized Nitrogen abundances ($12 + \log(N^+/H^+)$) for the sample with 0% overlap and that with 100% overlap. These average quantities are 8500 K, 25.8 cm^{-3} , and 7.95, for the sample without overlap, and 8450 K, 30.9 cm^{-3} , and 7.85, for the sample that fully overlaps with known H II regions. We find no significant dif-

Table 3. Nearest known H II region to sample LOS for $l \geq 0^\circ$.

LOS	H II Source	Distance	H II Radius	Beam overlap
		"	"	%
G000.0+0.0	G000.008+00.036	134.9	25.0	0
G000.5+0.0	G000.522-00.011	90.5	27.0	0
G003.5+0.0	G003.462-00.014	75.1	16.7	0
G004.3+0.0	G004.283+00.031	257.1	42.5	0
G005.2+0.0	G005.186-00.083	318.5	21.6	0
G006.1+0.0	G006.057-00.033	158.8	42.5	0
G007.8+0.0	G007.761+00.006	233.7	140.1	0
G008.7+0.0	G008.685-00.047	171.3	287.8	100
G010.4+0.0	G010.441+00.012	51.9	53.6	44
G011.3+0.0	G011.274-00.053	217.9	22.5	0
G012.2+0.0	G012.145-00.001	104.0	402.9	100
G013.0+0.0	G013.135+00.058	391.5	55.5	0
G013.9+0.0	G013.899-00.014	69.3	60.0	30
G014.8+0.0	G014.867+00.060	374.4	23.2	0
G016.5+0.0	G016.560+00.002	141.4	35.5	0
G020.0+0.0	G019.986+00.094	342.6	29.3	0
G020.9+0.0	G020.959+00.055	380.7	47.7	0
G021.7+0.0	G021.746-00.035	125.0	85.4	1
G023.5+0.0	G023.459-00.026	115.5	50.5	0
G024.3+0.0	G024.356+00.048	176.9	75.5	0
G025.2+0.0	G025.179+00.038	194.4	137.2	0
G026.1+0.0	G026.091-00.057	204.1	25.6	0
G027.0+0.0	G026.984-00.062	243.5	155.9	0
G028.7+0.0	G028.702+00.014	57.2	70.4	63
G030.0+0.0	G030.014+00.017	80.5	23.7	0
G031.3+0.0	G031.264+00.031	123.4	71.0	0
G036.4+0.0	G036.380+00.014	53.2	53.2	42
G037.7+0.0	G037.691+00.027	151.1	40.4	0
G041.5+0.0	G041.512+00.021	113.8	86.2	10
G044.0+0.0	G044.007-00.016	138.6	27.1	0
G045.3+0.0	G045.453+00.044	508.0	244.8	0
G049.1+0.0	G049.163-00.066	243.0	203.6	1
G054.3+0.0	G054.376-00.050	469.7	121.9	0

ference in the derived quantities depending on whether they overlap with a known H II region or not, suggesting that most of the sources in our sample are not associated with compact H II regions and are part of an extended, low ionization gas component at the outskirts of H II regions.

3. DISCUSSION

3.1. Nitrogen Abundance Determination

The ionized Nitrogen abundance, X_{N^+} , relative to ionized hydrogen is given by the ratio of the ionized Nitrogen, $N(N^+)$, and ionized hydrogen, $N(H^+)$, column densities (see also Pineda et al. 2019),

$$X_{N^+} = \frac{N(N^+)}{N(H^+)}. \quad (1)$$

Table 4. Nearest known H II region to sample LOS for $l < 0^\circ$

LOS	H II Source	Distance	H II Radius	Beam overlap
		"	"	%
G302.6+0.0	G302.586-00.029	156.6	64.2	0
G305.1+0.0	G305.201+00.009	343.6	27.6	0
G306.4+0.0	G306.361-00.291	1050.1	84.1	0
G307.7+0.0	G307.850+00.015	686.1	28.9	0
G310.2+0.0	G310.227-00.023	96.9	325.3	100
G314.0+0.0	G314.077+00.004	123.5	38.2	0
G316.6+0.0	G316.548-00.003	173.1	134.5	9
G317.9+0.0	G317.870-00.008	26.9	132.4	100
G326.8+0.0	G326.951+00.009	516.1	440.1	0
G330.0+0.0	G329.976-00.002	86.5	121.4	83
G331.7+0.0	G331.760+00.064	242.6	109.7	0
G332.6+0.0	G332.718-00.053	435.7	25.2	0
G333.5+0.0	G333.580+00.058	423.4	293.0	0
G336.1+0.0	G336.097+00.005	40.9	219.4	100
G337.0+0.0	G336.969-00.013	61.7	17.3	3
G337.8+0.0	G337.827+00.056	202.8	135.5	0
G338.7+0.0	G338.596-00.007	360.8	31.7	0
G342.2+0.0	G342.120+00.001	194.5	295.2	100
G343.9+0.0	G343.912+00.116	418.5	91.4	0
G345.7+0.0	G345.651+00.015	55.5	98.2	90
G346.5+0.0	G346.529-00.013	52.2	79.2	72
G349.1+0.0	G349.126+00.010	40.7	98.9	100
G350.9+0.0	G350.850-00.040	159.2	43.5	0
G353.5+0.0	G353.547-00.013	252.4	123.4	0
G354.3+0.0	G354.356+00.000	28.9	41.5	45
G355.2+0.0	G355.221-00.015	53.6	99.8	93
G356.1+0.0	G356.090-00.075	269.6	71.9	0
G359.5+0.0	G359.486+00.028	115.3	15.9	0

We derived the ionized Nitrogen column density from the [N II] 205 μ m line intensity ($I_{205\mu\text{m}}$) using (Goldsmith et al. 2015),

$$N(N^+) = \frac{4\pi I_{205\mu\text{m}}}{A_{10} h\nu_{205\mu\text{m}} f_1(n_e, T_e)}, \quad (2)$$

where the spontaneous decay rate (Einstein's A coefficient) is $A_{10} = 2.08 \times 10^{-6} \text{ s}^{-1}$, the rest frequency is $\nu_{205\mu\text{m}} = 1.461 \times 10^{12} \text{ Hz}$. The fractional population of the 3P_1 , f_1 , is a function of the electron density, n_e , and the electron temperature T_e .

In local thermodynamical equilibrium (LTE), the main-beam temperature (in units of K) per unit velocity (km s^{-1}) of a hydrogen recombination line is related to the emission measure, EM, (in units of $\text{cm}^{-6} \text{ pc}$), as (Rohlfis & Wilson 2004),

$$\int T^{\text{RRL}} dv = 5.76 \times 10^{11} T_e^{-3/2} EM \nu_{\text{RRL}}^{-1}, \quad (3)$$

where the speed of light, c , is in units of km s^{-1} , the rest frequency of the RRL, ν_{RRL} , in Hz, and the electron temper-

Table 5. Summary of Available Radio Continuum Surveys

I.D.	Frequency	Angular Resolution	Galactic Longitude Coverage	Reference
	[GHz]	[']		
VLA Galactic Center	0.332	0.72	$358^\circ < l < 2^\circ$	LaRosa et al. (2000)
HASLAM	0.408	51	Full Sky	Haslam et al. (1981)
VGPS	1.4	1	$18^\circ < l < 67^\circ$	Stil et al. (2006)
SGPS	1.4	1.6	$253^\circ < l < 358^\circ$	Haverkorn et al. (2006)
Effelsberg/GLOSTAR	4.88	2.4	$358^\circ < l < 60^\circ$	Brunthaler et al. (2021)
Parkes 64-m	5.0	4.1	$190^\circ < l < 40^\circ$	Haynes et al. (1978)
Effelsberg/GLOSTAR	6.82	1.8	$358^\circ < l < 60^\circ$	Brunthaler et al. (2021)
Nobeyama 45-m	10.3	2.66	$355^\circ < l < 56^\circ$	Handa et al. (1987)

ature, T_e , is in K. The EM is defined as the integral of the electron volume density squared along the line of sight,

$$EM = \int n_e^2 dl. \quad (4)$$

Assuming that the electron density is constant along the line of sight, which is approximately valid for the discrete sources we typically detect, this equation can be simplified to

$$EM = n_e N_e \simeq n_e N(\text{H}^+). \quad (5)$$

We can thus, re-order equation (3) in terms of the H^+ column density and electron density as,

$$N(\text{H}^+) = \int T^{\text{RRL}} dv / (1.87 \times 10^{-7} \nu_{\text{RRL}}^{-1} T_e^{-3/2} n_e), \quad (6)$$

where n_e is in units of cm^{-3} and $N(\text{H}^+)$ in units of cm^{-2} .

The hydrogen recombination line emission can be affected by deviations from local thermodynamical equilibrium and in this situation this deviation can be defined in terms of the ratio (Gordon & Sorochenko 2002),

$$G_{\text{LTE}}(n_e, T_c) = \frac{T^{\text{RRL}}}{T_{\text{LTE}}^{\text{RRL}}} = b_n \left[1 - \frac{1}{2} \tau_c \beta_n \right], \quad (7)$$

where b_n and β_n are the departure coefficient and amplification factor for a transition with principal quantum number n , respectively, and T_c and τ_c are the continuum brightness temperature and opacity, respectively, at ν_{RRL} . The continuum opacity can be derived from observations of T_c , and the electron temperature, using $\tau_c = T_c/T_e$. The effects of deviations from local thermodynamical equilibrium are well understood (Gordon & Sorochenko 2002) and a correction for these effects can be readily applied. We evaluated the brightness temperature of the continuum at the frequency of the RRL observations by extrapolating the synchrotron and free-free spectral energy distributions from the respective brightness temperature derived for each LOS, as described in Section 3.1.1.

The electron density can be calculated from the $[\text{N II}] 205 \mu\text{m}/122 \mu\text{m}$ intensity ratio and the electron temperature using Equations 21 and 22 in Goldsmith et al. (2015), for a range between 10 and 1000 cm^{-3} . The uncertainties in the determination of the electron density are determined by the uncertainty in the $[\text{N II}] 205 \mu\text{m}/122 \mu\text{m}$ intensity ratio and in those of the electron temperature.

3.1.1. Electron Temperature Determination

The electron temperature in optically thin, ionized gas regions that are in LTE can be derived from the ratio of radio recombination line (RRL) emission to thermal free-free radio continuum emission. This derivation is possible because RRL emission is proportional to the product of the emission measure (EM) and temperature to the power of -2.5 , while thermal radio free-free emission is proportional to EM times temperature to the power of -1.35 (Rohlf & Wilson 2004). As a result, the ratio of RRL to thermal radio continuum emission is proportional to temperature to the power of -1.15 and is independent of EM (e.g., Balsaer et al. 2015). The electron temperature is therefore given by,

$$\frac{T_e}{K} = \left[6.985 \times 10^3 \left(\frac{T_b}{T_L} \right) \left(\frac{\nu_{rc}}{\text{GHz}} \right)^{2.1} \cdot (\nu_{\text{RRL}}^{-1}) \cdot (\Delta\nu)^{-1} \cdot (1+y)^{-1} \right]^{0.86956}, \quad (8)$$

where T_b and T_L are the brightness temperatures of the free-free continuum and RRL peak intensity, respectively, $\Delta\nu$ is the RRL full width at half maximum, ν_{rc} is the frequency of the radio continuum emission, ν_{RRL} is the frequency of the RRL observations, and y is a term related to the contribution of $^4\text{He}^+$, which is assumed to be 0.08 (Balsaer et al. 2011).

There are several radio continuum surveys with a spatial coverage that overlaps that from our RRL survey and that have similar angular resolution, so that we can extract intensities for our analysis. These surveys include the VLA Galactic Plane Survey (Stil et al. 2006), the Southern Galactic Plane Survey (Haverkorn et al. 2006), the Nobeyama Radio Observatory 45-m telescope survey (Handa et al. 1987),

the Parkes 64-m telescope 6 cm survey³ (Haynes et al. 1978), and the Effelsberg 100-m part of the GLOSTAR survey (Medina et al. 2019; Brunthaler et al. 2021). In Table 5 we list the frequency, angular resolution and Galactic longitude coverage of these surveys. These surveys have varying angular resolutions and frequencies, and thus uncertainties in the relative calibration and the correction from the contribution from synchrotron emission can vary from survey to survey. To minimize these uncertainties, in each LOS we corrected all available continuum brightness temperatures for the contribution from synchrotron emission at their frequencies (see below), and estimated the continuum brightness temperatures at the frequency of our RRL observations, 8.5 GHz, assuming a free-free spectrum with spectral index of -2.1 . We then averaged all available samples together to obtain an average free-free brightness temperature at 8.5 GHz, which are listed in Tables 1 and 2. In our analysis, we only used radio continuum brightness temperatures with a signal-to-noise ratio larger than 10. In Appendix A we show the N^+/H^+ distribution as a function of Galactocentric distance derived using electron temperatures derived from each of the radio continuum surveys listed in Table 5 individually, showing that its distribution is not significantly affected by the choice of radio continuum survey used to derive electron temperatures.

We estimated the contribution of synchrotron emission at a given frequency using the 408 MHz map from Haslam et al. (1981) and assuming a synchrotron spectral index, in brightness temperature scale, of -2.8 . The 408 MHz map has an angular resolution of $51'$ which is significantly larger than that of our observations. Note however, that synchrotron emission in the Galactic plane is expected arise from diffuse spatially extended gas, while free-free emission originates from more compact and denser regions, so that we expect that uncertainties related to the difference in angular resolution are not significant. In the LOS toward the Galactic center region, where several compact non-thermal features are observed, we used the VLA 332 MHz map presented by LaRosa et al. (2000) convolved the angular resolution of our observations. We find that the typical contribution from synchrotron to the observed radio continuum brightness temperature in our sample is $\sim 47\%$ at 1.4 GHz, $\sim 40\%$ at 5 GHz, $\sim 36\%$ at 6.82 GHz, $\sim 26\%$ at 10.3 GHz.

As mentioned above, sources of uncertainties in using this derivation of the electron temperature include measurement uncertainties of the continuum and RRL emission, calibration uncertainties between the different frequency bands, the relative contribution from synchrotron and free-free emission to the observed continuum emission, and non-LTE effects for the RRL intensities. Note that pressure broadening is not expected to be significant in the density regime that we are sampling (Brocklehurst & Seaton 1972). We used the electron densities from the [N II] lines to account

for non-LTE effects on T_L using equation (7). In Appendix B, we compare our methodology to derive electron temperature against electron temperatures derived in a sample of H II regions by Balser et al. (2015) in which calibration uncertainties and synchrotron contribution are carefully assessed. We find that for electron temperatures derived using continuum at both 1.4 GHz and 6.82 GHz there is a scatter of about 20–30% which we attribute to the unaccounted uncertainties described above.

We also studied whether beam dilution effects resulting from using observations with different angular resolution in the RRL and continuum emission impact our determination of electron temperatures in our sample. To study beam dilution effects in the northern part of our sample, we smoothed the $60''$ VGPS survey at 1.4 GHz to the $84''$ and $160''$ resolutions of the GBT RRL and Nobeyama Radio Continuum data sets, respectively, and studied the intensity ratio at these two different angular resolutions. We found that beam filling effects are small for our sample, with typical variations smaller than 5%. To study beam dilution effects in the southern part of our sample, we also convolved the SGPS data at $100''$ to the $115''$ angular resolution of the DSS-43 data. We found small variations in the intensity ratio of the SGPS continuum data at $100''$ and $115''$ with typical variations smaller than 2%. Because the variation in intensities due to beam filling in our sample are small, suggesting that most sources are extended, we did not apply a beam filling correction to our data.

In Tables 7 and 8 we show the derived ionized Nitrogen abundances, electron densities, electron temperatures, and N^+ and H^+ column densities for our sample. In Figure 4 we show the distribution of these quantities as a function of Galactic longitude. As seen in Figure 4, the derived electron temperatures range between 3500 K and 21000 K, with an average value of $T_e = 8225$ K, which is typical of ionized gas regions, with a standard deviation of 3900 K. We notice that there is a dependence in the value of T_e with the signal-to-noise ratio of the RRL observations, with a tendency for temperatures to be higher at lower SNR values. The average temperature for $SNR > 10$ is 7484 K, while for $5 < SNR < 10$, it is 9343 K. This difference in the electron temperature has a small impact on the derived ionized Nitrogen abundances. Using Equations (1), (2), (6), and (8), for the observed range in ionized Nitrogen and RRL intensities, we can derive that N^+/H^+ is proportional to the electron temperature between $T_e^{-1.1}$ and $T_e^{-1.2}$. Because N^+/H^+ has an additional dependence on the RRL line intensity as T_L^{-1} (Equation 6), and the electron temperature depends on the RRL intensity as $T_L^{-0.87}$ (Equation 8), the resulting dependence of N^+/H^+ on the RRL intensity is weak ($\sim T_L^{-0.04}$). Thus, an uncertainty of a factor of 2 arising from T_L would impact T_e by the same factor but N^+/H^+ by only a factor of 1.03. Note however, that N^+/H^+ is proportional to $\sim T_b^{-1}$, and therefore uncertainties from the continuum intensity can have a larger impact in the derived Nitrogen abundance. This result motivated us to adopt a larger $SNR > 10$ criterion for selecting lines-of-sights from the radio continuum data set.

³ Data from the Nobeyama 45-m and Parkes 64-m surveys are, among other Galactic plane surveys, available for download at the MPIFR's survey sampler at <https://www3.mpifr-bonn.mpg.de/survey.html>.

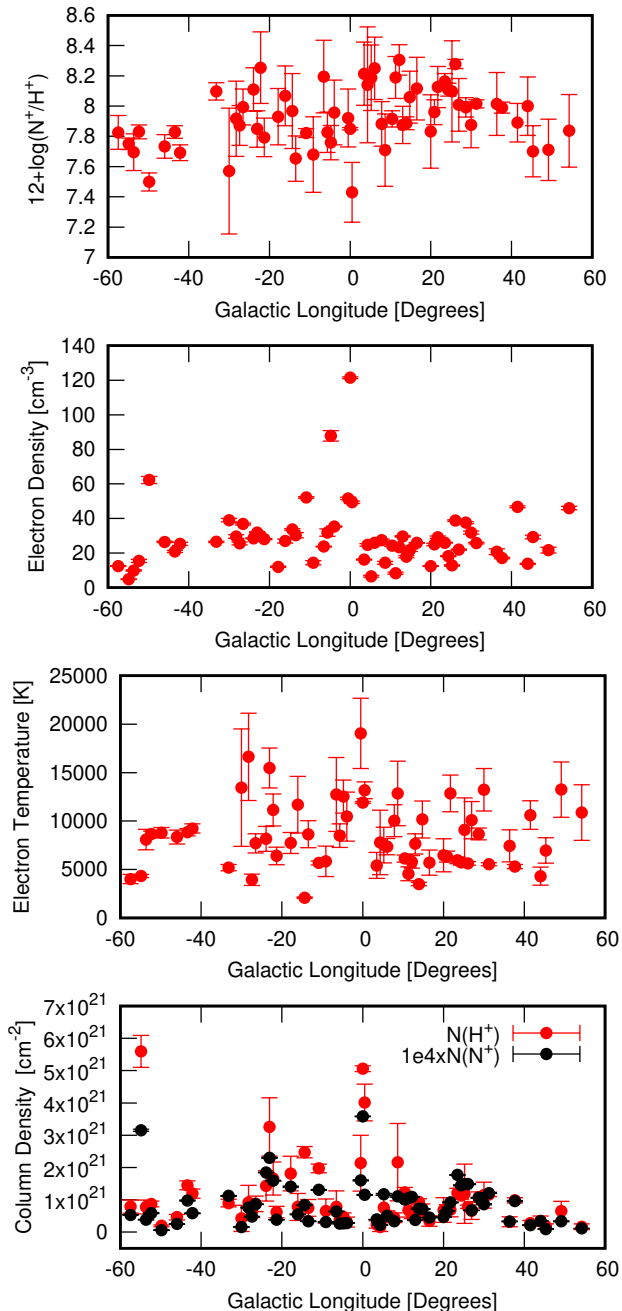


Figure 4. Derived ionized Nitrogen abundances, electron densities, electron temperatures, and N^+ and H^+ column densities as a function of Galactic longitude.

3.1.2. The ionization structure of Nitrogen

The ionization potential of Nitrogen (14.53 eV) is greater than that of hydrogen (13.60 eV) by 0.93 eV, so Nitrogen can be in neutral form in regions where Hydrogen is fully ionized by photons between 13.60 eV and 14.53 eV. In the ISM, four primary processes contribute to Nitrogen ionization: EUV (14.53 eV to 124.24 eV) photoionization, electron collisional ionization, proton (H^+) charge transfer, and X-ray photoion-

ization. While electron recombination with N^+ serves as the primary loss mechanism (Langer & Pineda 2015; Langer et al. 2021). Models show that electron collisional ionization of Nitrogen alone is inefficient at temperatures below $\sim 10^4$ K due to the large ionization potential of atomic Nitrogen. However, proton charge transfer ($H^+ + N \rightarrow H + N^+ - 0.93$ eV), which has a smaller energy barrier, might be important at temperatures above 5000 K (see Section 4 in Langer & Pineda 2015 and Langer et al. 2021). Therefore a significant fraction of Nitrogen might be ionized even where few EUV photons are present above 14.54 eV due to collisional and exchange ionization by electrons and protons, respectively. Note, however, that a medium where Nitrogen is fully ionized is difficult to attain without EUV photons because collisional ionization with electrons or charge exchange with protons is generally balanced by electron recombination and therefore roughly independent of electron density (Langer et al. 2021). It is only where EUV dominates ionization that an increase in photon flux can eventually overcome electron recombination leading to a fully ionized Nitrogen gas.

Under typical ISM and H II region conditions, higher ionization states of Nitrogen, such as N^{++} , can be maintained only by the presence of an EUV field. Models show that an electron temperature greater than about 25000 K is required for collisional ionization to be important. Thus, under typical temperatures and densities of the ionized gas, as determined here, N^{++} will not have a significant abundance without a source of EUV photons, such as are typically present in the close vicinity of massive stars. This result suggests that regions with higher ionization levels than N^+ , such as can be probed with the $[N III] 57\mu m$ line, are likely to be compact and closely associated with H II regions. It is possible, however, that EUV photons leakage from H II regions (Luisi et al. 2019) might make a more diffuse, extended component of highly ionized Nitrogen possible (Mizutani et al. 2002).

If a significant fraction of the gas-phase Nitrogen is at ionization levels higher than N^+ , our assumption that the N/H abundance ratio can be traced by the N^+/H^+ abundance ratio might not be valid, and therefore it introduces uncertainties into our analysis. Note that the linear correlation between the $[N II]$ and RRL lines shown in Figure 2 suggest that if there is any underestimation of the total Nitrogen along the line-of-sight, the effect is not significant.

To determine whether higher ionization states, such as N^{++} , might be a significant source of Nitrogen in our sample, we used SOFIA and *Herschel* observations of the fine structure line of doubly ionized Nitrogen $[N III] 57\mu m$, to characterize the ionization environment of 8 LOS in our survey, and in the Sgr A region in the Galactic center. Under the typical physical conditions of our LOS sample (temperatures less than 20,000 K), N^{++} can only be maintained by EUV photons from massive stars. Therefore, the presence of $[N III]$ will enable us to determine whether EUV photons play an active role in determining the ionization structure of Nitrogen in our sample.

The $[N III] 57\mu m$ line was detected in 4 out of the 8 LOS, and their intensities, and 3σ upper limits in case of the non-

detections, are listed in Table 1 and the detected spectra are shown in Figure 3. As we can see in Table 3, these LOS are either inside (G010.4+0.0 and G028.7+0.0), or in the close vicinity of (G000.0+0.0 and G024.3+0.0), dense H II regions cataloged with WISE. This association suggests that their environments can be influenced by EUV photons that can further ionize N^+ to N^{++} .

In Table 6, we present the results of our analysis of the [N III] 57 μ m observations. We derived N^{++} column densities from the observed [N III] 57 μ m intensity and the electron density derived from the [N II] 122 μ m/205 μ m ratio using,

$$N(N^{++}) = \frac{4\pi I_{57\mu\text{m}}}{A_{ul} h \nu_{57\mu\text{m}} f_{3/2}(n_e)}, \quad (9)$$

where the spontaneous decay rate for N^{++} is $A_{ul} = 4.79 \times 10^{-5} \text{ s}^{-1}$, and the rest frequency is $\nu_{57\mu\text{m}} = 5.229 \times 10^{12} \text{ Hz}$. The fractional population of the $^{1/2}P_{1/2}$, $f_{3/2}$, is a function of the electron density, n_e , as shown in Figure 5. The derived N^{++}/N^+ ratio for the detected sources ranges from 0.09 to 0.87, suggesting that doubly ionized Nitrogen in these regions is not dominant, but could be a significant fraction of the total Nitrogen, and thus can introduce an underestimation of the total Nitrogen abundance derived from N^+/H^+ between factors of ~ 1.09 for G000.0+0.0 and ~ 1.87 in G010.4+0.0. A similar range is obtained for the 3σ upper limits. However, these results are based on the assumption that the electron density of the [N III]–emitting region is the same as that of the [N II]–emitting region, whereas, given the EUV requirements to produce N^{++} , it is more likely that [N III] comes from compact regions closer to the source of H II regions. Thus, under these assumptions, the derived N^{++}/N^+ ratio should be considered as an upper limit. As we can see in Figure 5, for the typical densities derived from the Nitrogen lines ($\sim 20\text{--}100 \text{ cm}^{-3}$), the population of the $^{1/2}P_{3/2}$ level is very small ($< 10\%$), and thus a relatively large N^{++} column density is needed to reproduce the observed [N III] 57 μ m intensities and upper limits. For $T_e=8000 \text{ K}$, the $^{1/2}P_{3/2}$ level is 50% populated at about 1000 cm^{-3} , and assuming such a density in our analysis would result in a N^{++} column density and N^{++}/N^+ ratio that are a factor of ~ 10 lower than those resulting from electron densities determined from the [N II] 122 μ m/205 μ m ratio. A more appropriate tracer of the volume density of gas associated with doubly ionized Nitrogen is the [O III] 52 μ m/88 μ m ratio, as the critical density of the [O III] 52 μ m line is similar to that for [N III] 57 μ m, as is the EUV requirement to produce O^{++} .

The Sagittarius A region in the Galactic center was observed in the [N II] 122 μ m and 205 μ m and the [O III] 52 μ m and 88 μ m lines by *Herschel*/PACS and represents an ideal location to study the ionization structure of Nitrogen without uncertainties in the volume density determination. We used both the [N II] 122 μ m/205 μ m ratio and the [O III] 52 μ m/88 μ m line ratios to derive the electron volume density in the low and high ionization regions, respectively. We followed the procedure discussed in Section 3.1 and used the

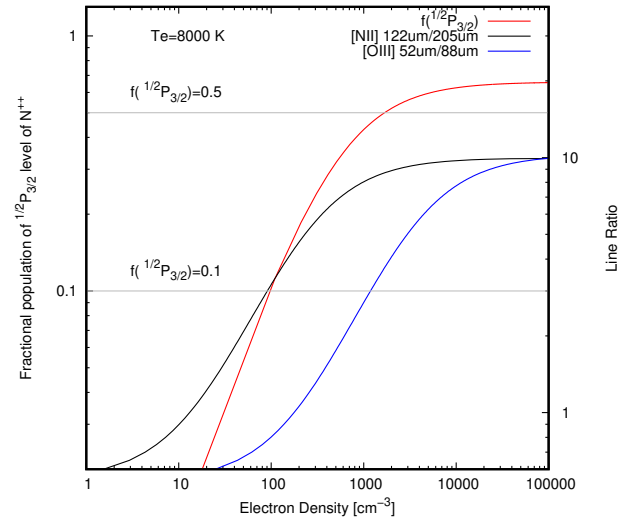


Figure 5. Fractional population of the $^{1/2}P_{3/2}$ level of N^{++} , and [N II] 205 μ m/122 μ m and [O III] 52 μ m/88 μ m line ratios, as a function of the electron density for an electron temperature of 8000 K. The horizontal lines highlight the electron densities at which the fractional level populations are 10% and 50%.

ratio of the X–band continuum brightness temperature determined from the GBT, and the H92 α Hydrogen recombination line data presented by Wong et al. (2016), including a correction for the contribution of Synchrotron emission, to derive an electron temperature of 11443 K (see Table 6). We derive an electron density of 254 cm^{-3} from the [N II] lines, and 2874 cm^{-3} , from the [O III] lines. Using the derived volume densities for low ([N II]) and high ([O III]) ionization regions, and the electron temperature, we calculated a column density of singly ionized Nitrogen of $6.3 \times 10^{17} \text{ cm}^{-2}$ and of doubly ionized Nitrogen $3.7 \times 10^{16} \text{ cm}^{-2}$. We find that N^{++} represents only a small fraction (6%) of the total $N^+ + N^{++}$. Thus, when appropriate electron densities are used for the different ionization regimes, we find that most of the ionized gas mass in this region is at a low ionization state where most of the Nitrogen is singly ionized. Using the parameters derived above, and assuming that the emission measure from the RRL lines can be separated between that arising from low and high ionization regions using the 6% ratio derived for Nitrogen, we derive a Nitrogen abundance for this region of $12 + \log(N/H) = 7.86$, which is consistent to those derived in our sample for the Galactic center.

3.1.3. Galactocentric Distance Determination

Because our sample in the inner Galaxy is uniformly distributed in Galactic longitude, we expect that the LOS analyzed here have a wide range of galactocentric distances in the inner Galaxy, so that we can study the radial distribution of the ionized Nitrogen abundance in the Milky Way. The traditional method for determining the Galactocentric distances from sources in the Galactic plane is the use of kinematic distances derived from the LSR velocity and Galactic coordinates of the source. However, because of non circular mo-

Table 6. Single and Doubly ionized Nitrogen Column Densities

LOS	T_e [K]	n_e ([N II]) [cm^{-3}]	$N(\text{N}^+)$ [10^{17}cm^{-2}]	n_e ([O III]) [cm^{-3}]	$N(\text{N}^{++})$ [10^{17}cm^{-2}]	$N(\text{N}^{++})/N(\text{N}^+)$
G000.0+0.0	11910 ± 97	121.47 ± 0.52	3.58 ± 0.01	–	0.32 ± 0.05	0.09 ± 0.01
G007.0+0.0	8000 ± 800	32.77 ± 0.66	0.81 ± 0.01	–	$<0.43 \pm 0.14$	$<0.53 \pm 0.18$
G010.4+0.0	6129 ± 367	24.32 ± 0.51	1.01 ± 0.01	–	0.88 ± 0.10	0.87 ± 0.10
G012.2+0.0	5800 ± 648	23.35 ± 0.43	1.09 ± 0.01	–	$<0.65 \pm 0.22$	$<0.60 \pm 0.20$
G023.5+0.0	5949 ± 339	25.99 ± 0.25	1.77 ± 0.01	–	$<0.55 \pm 0.18$	$<0.31 \pm 0.10$
G024.3+0.0	5744 ± 276	18.15 ± 0.29	1.45 ± 0.01	–	1.15 ± 0.16	0.80 ± 0.11
G026.1+0.0	5630 ± 198	38.83 ± 0.42	1.49 ± 0.01	–	$<0.71 \pm 0.24$	$<0.47 \pm 0.16$
G028.7+0.0	8663 ± 612	37.62 ± 0.56	1.06 ± 0.01	–	0.48 ± 0.05	0.45 ± 0.05
SGRA	9601 ± 367	237.63 ± 27.43	6.34 ± 0.63	2686.6 ± 1027.9	0.37 ± 0.01	0.06 ± 0.01

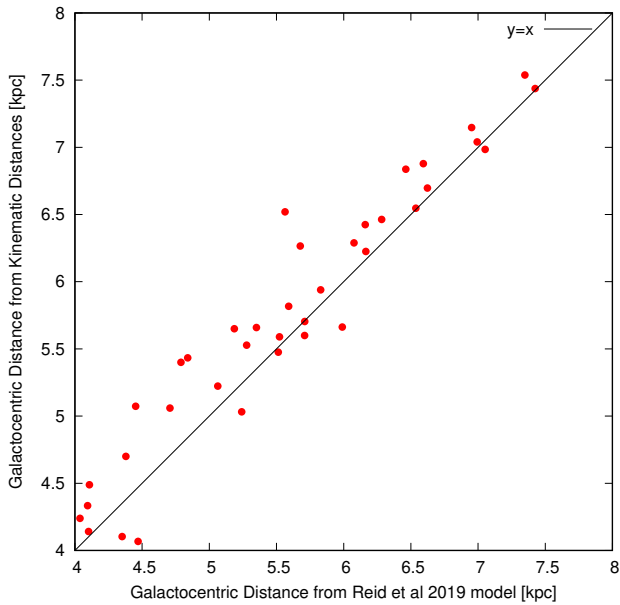


Figure 6. Comparison between Galactocentric distances determined using the Reid et al. (2019) model and those derived from kinematic distances. Only data points with $R_{\text{gal}} > 4$ kpc are shown, as kinematic distances are not accurate for non-circular motions observed in sources associated with the Galactic bar in the innermost part of the Galaxy.

tions associated with the Galactic bar, kinematic distances cannot be accurately determined in the inner $R_{\text{gal}} \lesssim 4$ kpc of the Galaxy.

To ensure that we are able to sample the Galactic plane in the innermost parts of the Galaxy and the Galactic center, we instead use the model of the Galaxy presented by Reid et al. (2019, see also Reid et al. 2016) to determine the Galactocentric distances to the sources detected in our survey. Reid et al. (2019) presented a model of the spiral structure of the Milky Way based on 200 trigonometric parallaxes of masers associated with massive star forming regions. Distances measured

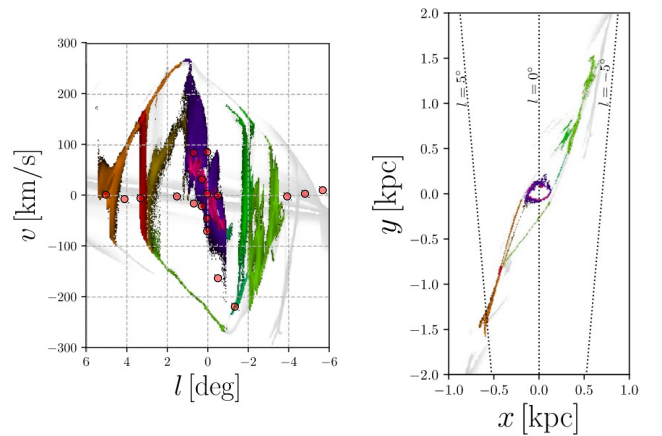


Figure 7. Gas kinematics in the longitude–velocity map (*left*) and corresponding spatial distribution (*right*) of the Galactic center region predicted by numerical simulations of gas flows in a barred potential presented by Sormani et al. (2019). We overplotted the fitted velocity of the RRLs for the 18 LOSs in our survey in this region as orange dots.

from maser trigonometric parallaxes have the advantage that they do not rely on any assumption on the kinematics of the Galaxy. The Reid et al. (2019) model enables us to estimate distances to sources using their Galactic coordinates and LSR velocity. From a distance, D , to a source with Galactic longitude l and latitude $b = 0^\circ$, the corresponding Galactocentric distance is given by,

$$R_{\text{gal}} = \sqrt{D^2 - 2R_\odot D \cos(l) + R_\odot^2}, \quad (10)$$

where R_\odot is the distance from the Sun to the Galactic center which is fitted to be $R_\odot = 8.15$ kpc by Reid et al. (2019).

In Figure 6, we show a comparison between Galactocentric distances derived for our sample using the Reid et al. (2019) model and those derived from kinematic distances, for $R_{\text{gal}} > 4$ kpc. The kinematic distances are determined for a given velocity component with Galactic longitude l , latitude

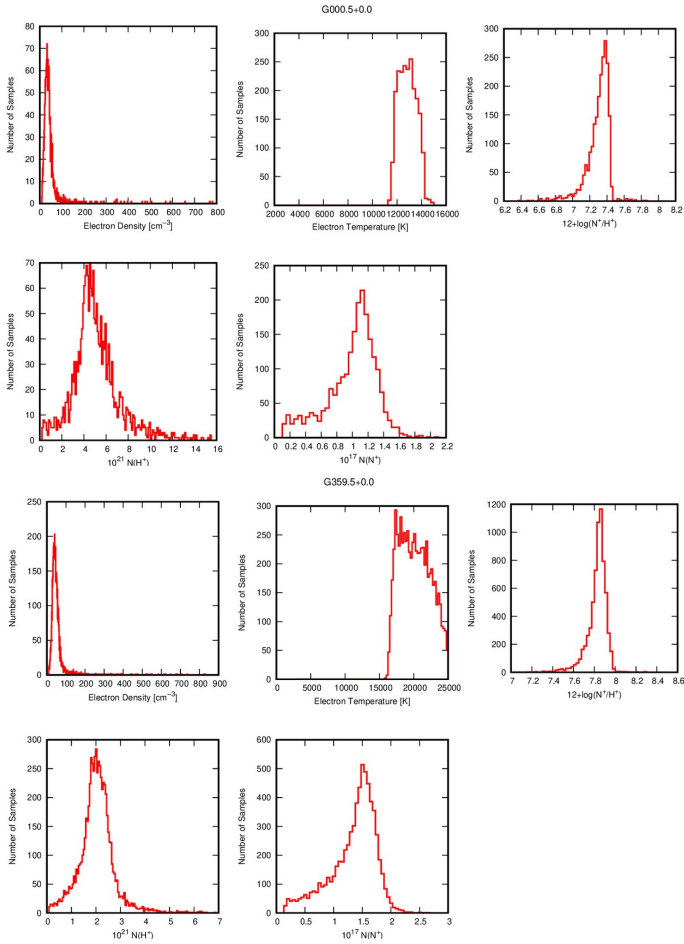


Figure 8. Sample solutions for N^+/H^+ and constrained values of the electron density, electron temperature, and N^+ and H^+ column density for G000.5+0.0 and G359.5+0.0 using the procedure described in Section 3.1.3.

b , and local standard of rest (LSR) velocity V_{LSR} , is given by

$$R_{\text{gal}} = R_{\odot} \sin(l) \cos(b) \left(\frac{V(R_{\text{gal}})}{V_{\text{LSR}} + V_{\odot} \sin(l) \cos(b)} \right), \quad (11)$$

where V_{\odot} is the orbital velocity of the Sun with respect to the Galactic center, and $V(R_{\text{gal}})$ is the rotation curve. We assume a “Universal” rotation curve presented by Persic et al. (1996) (see Equation 3 in Wenger et al. 2018) assuming the value of the Sun’s rotation velocity, $V_{\odot} = 247 \text{ km s}^{-1}$, fitted by Reid et al. (2019). We tested the dependence of R_{gal} with other determinations of V_{\odot} (Zhou et al. 2023; Akhmetov et al. 2024), finding negligible differences. As we can see, the Reid et al. (2019) model is in very good agreement with Galactocentric distances derived from kinematic distances, with values of R_{gal} derived from the Reid et al. (2019) model being on average $\sim 5\%$ lower than those derived from kinematic distances.

There are 24 LOS in our sample that have a single RRL velocity component enabling us to directly associate this emission with the velocity–unresolved [N II] 205 μm and 122 μm

and radio continuum emission. In case of multiple component LOS, we determined R_{gal} for each velocity component and determined the range of galactocentric distances that these velocities represent. We assume that the N^+/H^+ gradient is smooth at $< 1.5 \text{ kpc}$ scales and thus we can assume that the velocity components in given LOS have the same Nitrogen abundance in case they are at least within 1.5 kpc from each other. There are 14 LOS in this category for which the relative distance between the two components is lower than 1.5 kpc. For this sub sample, we assigned the average radial distance to the derived ionized Nitrogen abundance and considered the radial range as error bars in the X–axis.

There is a subset of 8 LOS, mostly located in the inner $\pm 20^\circ$ from the Galactic center, where a high LSR velocity component with $v_{\text{LSR}} > \pm 80 \text{ km s}^{-1}$ together with another low LSR velocity at about $v_{\text{LSR}} \simeq 0 \text{ km s}^{-1}$, are observed. The Reid et al. (2019) model suggests that the low velocity components are at distances larger than 4 kpc from the Galactic Center while the components with high LSR velocity are in the $0 \text{ kpc} < R_{\text{gal}} < 4 \text{ kpc}$ range. Thus, the high LSR velocity components are likely associated with the Galactic bar and located in the proximity of the Galactic center. In Figure 7, we show the result of numerical simulations of gas flows in a barred potential presented by Sormani et al. (2019), with the left panel showing the predicted gas kinematics in the longitude–velocity map of this region and in the right panel the spatial distribution of these different components. We overplotted the fitted velocity of the RRLs for the 18 velocity components in our survey in this region as orange dots. As we can see the high LSR velocity components are likely associated with the bar potential gas corresponding to the inner 2 kpc of the Galaxy. At the same time, sources with velocities near $v_{\text{LSR}} \simeq 0 \text{ km s}^{-1}$ are likely at higher Galactocentric distances. In the figure, we see that the G000.0+0.0 LOS shows multiple velocity components which are predicted to be associated with the Galactic center. We therefore assume for this LOS that the N^+/H^+ , electron temperature, and electron density of the gas is the same for all velocity components, and therefore we can combine the RRL data with the unresolved PACS and continuum data to derive N^+/H^+ .

Because the observed velocity unresolved [N II] 122 μm and 205 μm emission is the sum of the intensity of these lines arising from both velocity components, to determine the N^+/H^+ in the high LSR velocity sources we need to estimate the contribution to the observed [N II] intensity from the low LSR velocity sources. As discussed above, the Reid et al. (2019) model suggests that the low velocity components are at distances larger than 4 kpc from the Galactic Center. If that is the case, we can assume that the N^+/H^+ for the low LSR velocity sources is within the range observed for all other sources across the Galaxy with $R_{\text{gal}} > 4 \text{ kpc}$, and we can determine its value using the fit to the N^+/H^+ distribution as a function of Galactocentric distance derived below (Equation 16). With an assumed N^+/H^+ , the intensity of the [N II] 122 μm and 205 μm emission for the low velocity component

is given by,

$$I_{122\mu\text{m}}^{\text{low}} = \frac{A_{21}h\nu_{122\mu\text{m}}X_{\text{N}^+}EMf_2(ne, T_e)}{4\pi ne} \quad (12)$$

and

$$I_{205\mu\text{m}}^{\text{low}} = \frac{A_{10}h\nu_{205\mu\text{m}}X_{\text{N}^+}EMf_1(ne, T_e)}{4\pi ne} \quad (13)$$

where f_1 and f_2 are the level populations of the $^3\text{P}_1$ and $^3\text{P}_2$ levels, respectively, and the EM is derived from the RRL observations for this velocity component using Equation (3). As we can see the intensities of these sources depend on the electron density and temperature of the low velocity component. With the derived [N II] 122 μm and 205 μm intensities of the low velocity component we can obtain

$$I_{122\mu\text{m}}^{\text{high}} = I_{122\mu\text{m}} - I_{122\mu\text{m}}^{\text{low}} \quad (14)$$

and

$$I_{205\mu\text{m}}^{\text{high}} = I_{205\mu\text{m}} - I_{205\mu\text{m}}^{\text{low}}, \quad (15)$$

and the electron density for the high velocity component is derived from the [N II] 122 μm /205 μm ratio and an electron temperature. With the intensity of either the [N II] 122 μm or 205 μm lines, the electron temperature, density, and the measured EM from the RRL, we can derive the ionized Nitrogen abundance using Equation (1),(2), and (6).

Note however, that the electron temperatures and densities of each LSR velocity component cannot be independently derived. This is because both [N II] 122 μm and 205 μm and radio continuum intensities, which are used to determine the electron density and temperature, respectively, are velocity unresolved and thus correspond to the sum of the intensities arising from each velocity component. To investigate the range of possible solutions for the N^+/H^+ ratio for the high velocity component given these uncertainties, we evaluated this quantity using the method described above, for ranges in the electron temperature, for the low and high LSR velocity components, from 1000 K to 25000 K, of the [N II] 122 μm /205 μm ratio, corresponding to $n_e=10\text{--}1000\text{ cm}^{-3}$. Additionally, we assumed a range for the N^+/H^+ ratio for the low LSR velocity component that corresponds to the typical standard deviation for $R_{\text{gal}} > 4\text{ kpc}$ of a factor of 2. Using 10^6 combinations of these parameters, we solved for the N^+/H^+ abundance ratio of the high velocity component. These solutions were constrained using the measured values of the continuum temperature and the [N II] 205 μm and 122 μm lines. We used Equation (8) to, given the known RRL intensity of each component, estimate the continuum brightness temperature of each component that would result from a given temperature, with the constraints that the continuum brightness temperature of each source has a SNR above 5 and that the sum of the resulting continuum brightness temperatures of each component is equal to the measured value within its uncertainties. Additionally, for a given [N II] 122 μm /205 μm ratio and temperature for the low LSR component, we determined the corresponding electron

density. With the electron density, electron temperature, and the N^+/H^+ ratio for this velocity component, we evaluated the [N II] 205 μm and 122 μm line intensities using Equations (12) and (13). We then used Equations (14) and (15) to evaluate the corresponding [N II] intensities and electron density of the high LSR velocity component, for a given electron temperature for this velocity component. The solutions were constrained requiring that the derived [N II] intensities for the high and low LSR velocity components have each a SNR above 5, and that the sum of the [N II] lines from these components match the observed values within their uncertainties. In Tables 7 and 8 we list the average value of all possible solutions for N^+/H^+ and the constrained values of the electron temperature, electron density, and N^+ and H^+ column densities, for the high LSR velocity component together with their corresponding standard deviation. In Figure 8, we show two examples of the derived N^+/H^+ and constrained parameters, showing that this approach results in well constrained parameters.

3.2. The distribution of Nitrogen abundances in the disk of the Milky Way.

In Figure 9, we show the distribution of Nitrogen abundances as a function of Galactocentric distance derived from our sample in the range from 0 to 8 kpc in the inner Galaxy. We used only data with RRL emission above a SNR of 5, and a radio continuum brightness temperature used to determine the electron temperature with SNR above 10. These criteria result in a sample of 41 positions for which we consider the data to be of high quality. We also show, in dark green, the Nitrogen abundance derived in Sgr A and discussed in Section 3.1. We also include a sample of Nitrogen abundances derived in 42 H II regions presented by [Arellano-Córdova et al. \(2021\)](#), using optical spectral lines, sampling the Galactic plane from 4 to 17 kpc. We find that the Nitrogen abundances derived here and those those derived with optical spectral line observations are in excellent agreement in the Galactocentric distance region they overlap. Taken together, these data sets represent a continuous sample of the Nitrogen abundance over the disk of the Milky Way from 0 to 17 kpc.

Both our Nitrogen abundances and those from [Arellano-Córdova et al. \(2021\)](#) are determined in low ionization regions that have a negligible fraction of doubly ionized Nitrogen. Therefore we can assume for both data sets that $\text{N}/\text{H} \approx \text{N}^+/\text{H}^+$. The agreement between our Nitrogen abundances and those derived using optical data is in contrast to discrepancies between FIR and optical derived abundances and the N/O ratio as reported by [Rudolph et al. \(2006\)](#) and [Arellano-Córdova et al. \(2021\)](#). [Arellano-Córdova et al. \(2021\)](#) compared the optical based observations of the N/H abundance gradient with those derived using mid- and far-infrared observations by [Rudolph et al. \(2006\)](#) finding that the latter show a significantly steeper gradient and larger dispersion, compared to those derived with optical lines. A possible explanation for this discrepancy is that [Rudolph et al. \(2006\)](#) abundance determination is based on observations of spectral lines tracing high ionization states, such as [N III]

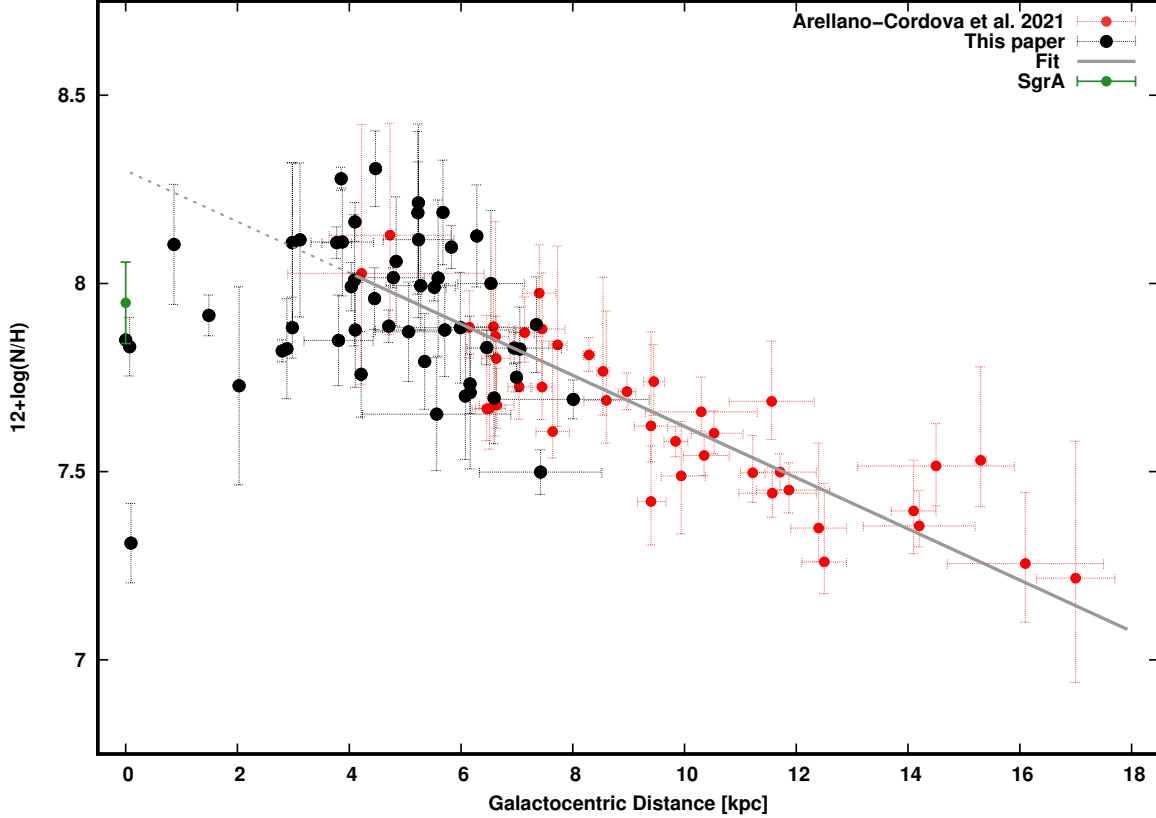


Figure 9. The distribution of Nitrogen abundances as a function of Galactocentric distance. We show our sample ranging from 0 to 8 kpc in the inner galaxy. We also include data points presented by Arellano-Córdova et al. (2021) sampling the Solar neighborhood and Outer galaxy from 6 to 17 kpc. These datasets together represent a continuous sample of the Nitrogen abundance over the disk of the Milky Way from 0 to 17 kpc. We also show the ionized Nitrogen abundance derived in Sagittarius A and discussed in Section 3.1 in dark green.

and [O III] lines, and therefore they rely in a correction factor for lower ionization gas that can introduce significant uncertainties in the measurements.

In the left panel of Figure 10 we show the ionized Nitrogen abundances as a function of Galactocentric distance separated into the different cases in which they were derived, with single velocity components shown in red, double components in black, triple components in green, and LOS associated with the central molecular zone shown in yellow. In the right panel of Figure 10 we show the ionized Nitrogen abundance as a function of Galactocentric distance separated from those derived for LOS with $l \geq 0^\circ$ (black) and $l < 0^\circ$ (blue). We find that the ionized Nitrogen abundances for LOS with $l \geq 0^\circ$ are on average 40% larger than for $l < 0^\circ$. This difference coincides with a similar asymmetry in the star formation rate distribution in the Milky Way (Elia et al. 2022), suggesting that metal production is enhanced in the region with $l \geq 0^\circ$ compared to that for $l < 0^\circ$.

We find that the Nitrogen abundance in the Milky Way decreases from about 4 kpc out to 17 kpc, while having a flat distribution from 4 kpc to the Galactic center. Observations of Cepheids and red giants also show that different elements, including iron (Fe), have abundances close to the Galactic center that are lower than predicted by extrapolating the abundance distribution at larger radii (Davies et al. 2009; Na-

jarro et al. 2009; Hayden et al. 2014; Martin et al. 2015; Andrievsky et al. 2016), in agreement with our results. We did not attempt to fit our data in the $4 \text{ kpc} < R_{\text{gal}} < 8 \text{ kpc}$ range, as this range is too narrow for enabling an accurate representation of N/H across the Milky Way. Instead, we combined our data set with that from Arellano-Córdova et al. (2021) to obtain a fit to the distribution of Nitrogen abundance in the Galactic plane between 4 kpc and 17 kpc. We used the orthogonal bi-variate error and intrinsic scatter method (BES Akritas & Bershady 1996), including a bootstrap resampling error analysis, resulting in,

$$12 + \log(\text{N}^+/\text{H}^+) = 8.30 \pm 0.04 - (0.068 \pm 0.005)R_{\text{gal}}. \quad (16)$$

The slope of our fit is consistent within its uncertainties to that derived by Arellano-Córdova et al. (2021), $-0.057 \text{ dex kpc}^{-1}$, using optical lines, but is shallower than that derived by Pineda et al. (2019), $-0.076 \text{ dex kpc}^{-1}$, using the same method presented here in a smaller sample of 11 LOS, and that derived by Rudolph et al. (2006), $-0.085 \text{ dex kpc}^{-1}$. The slope of our fit is steeper than that derived for O/H by Arellano-Córdova et al. (2021), $-0.042 \text{ dex kpc}^{-1}$. This difference can be understood as a larger number of older intermediate mass stars, that can contribute additional Nitrogen to the ISM, are present in the

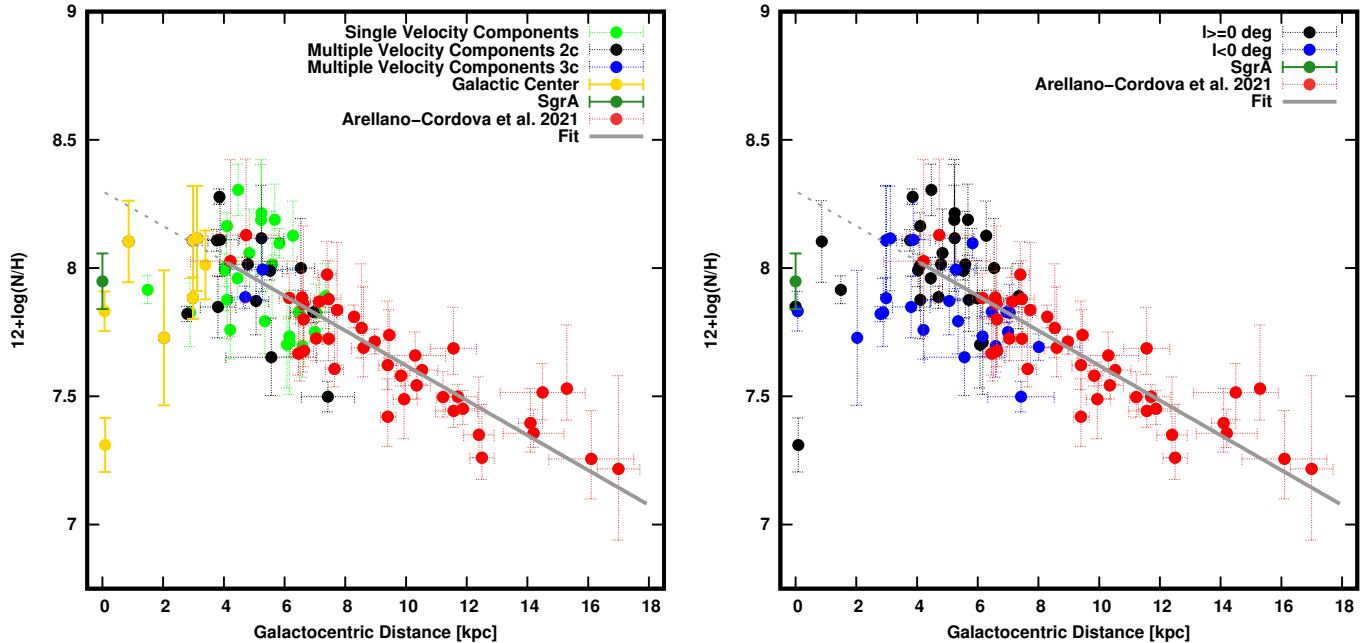


Figure 10. (*left*) Ionized Nitrogen abundances as a function of Galactocentric distance separated in the different cases in which they were derived, with single velocity components shown in green, double components in black, triple components in green, and LOS associated with the central molecular zone in shown in yellow. We also show the ionized Nitrogen abundance derived in Sgr A and discussed in Section 3.1 in dark green. (*right*) Ionized Nitrogen abundances as a function of Galactocentric distance separated between those derived from LOS with $l \geq 0^\circ$ (black) and $l < 0^\circ$ (blue).

inner Galaxy. The typical dispersion from the fit for our data set for $R_{\text{gal}} > 4$ kpc is 0.16 dex and 0.14 dex when also considering the data set from Arellano-Córdova et al. (2021). These dispersions are somewhat larger than those reported by Arellano-Córdova et al. (2021), of 0.1 dex, but are consistent with the suggestion from this work that azimuthal variations are not significant for Nitrogen.

Note that in Pineda et al. (2019) we assumed electron temperatures from Balsa et al. (2011) instead of deriving them using radio continuum data as is done here. The Balsa et al. (2011) electron temperature gradient was derived from H II regions between 5 kpc and 8 kpc, but we extrapolated the fit down to the Galactic center. Data presented by Quireza et al. (2006) show electron temperatures in the Galactic center that are significantly larger than predicted by extrapolating the fit from electron temperatures at larger Galactocentric distances inward to $R_{\text{gal}}=0$ kpc. This underestimation of the electron temperature at the Galactic center resulted in an overestimation of the Nitrogen abundances in this region as found by Pineda et al. (2019).

3.2.1. Comparison with chemical evolution models of the Milky Way.

Metallicity gradients in the disk of Galaxies are formed when star formation is more efficient in their inner parts compared with their outer parts (Matteucci 2021). Such a gradient in the star formation efficiency can be produced by “inside-out” galaxy formation, in which the disk of galaxies form by gas accretion with a rate that is faster in the in-

ner Galaxy compared with the outer Galaxy (Larson 1976; Matteucci & Francois 1989; Boissier & Prantzos 1999; Pilkington et al. 2012). In these models, the measured slope of the gradient constrains the galaxy accretion rate. However, other mechanisms can also predict and/or steepen a metallicity gradient such as the presence of a density threshold for star formation, a star formation efficiency that decreases with Galactocentric distances, and inwards radial flows (Kubryk et al. 2015; Palla et al. 2020; Grisoni et al. 2021). Palla et al. (2020) presented set of chemical evolution models of the Milky Way that assume a two-infall model (Chiappini et al. 1997; Romano et al. 2010), in which the thick and thin disks were formed in two accretion episodes separated by ~ 3.25 Gyr, to study the abundance distribution of several elements as a function of Galactocentric distance. These models that include the effects of radially variable star formation efficiency (SFE) and radial flows in addition to inside-out growth in the determination of the radial distribution of element abundances in the Milky Way. The mechanism by which a variable SFE induces and/or steepen an abundance gradient is that in the innermost regions of galaxies the star formation rate is enhanced compared to the outer regions, leading to an increased chemical enrichment. Additionally, radial flows can contribute to this effect. As gas moves toward the inner parts of the galaxy, the star formation rate increases, resulting in more significant metal production closer to the center compared to the outer areas.

In Figure 11 we compare the observed Nitrogen abundance distribution with the models presented by Palla et al. (2020)

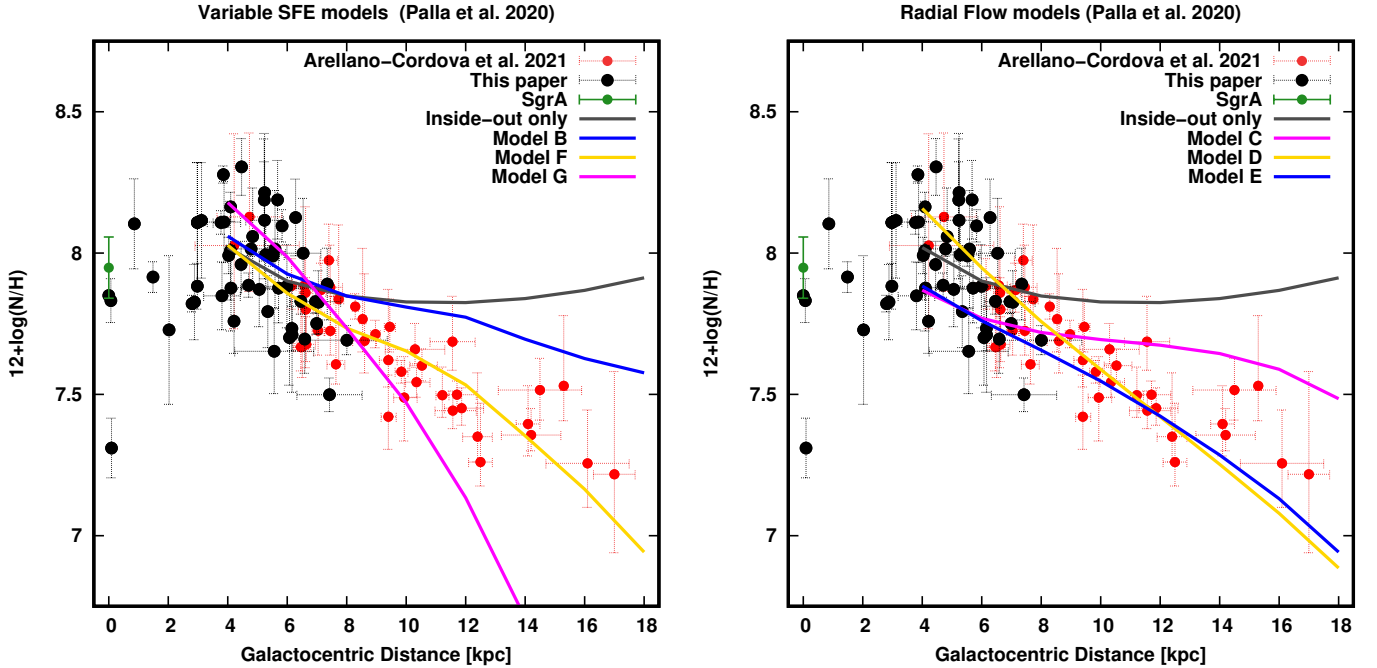


Figure 11. Comparison between the observed Nitrogen abundance distribution as a function of Galactocentric distance and model calculations presented by Palla et al. (2020) for $R_{\text{gal}} > 4$ kpc. These models include a prediction of inside-out growth only (dark grey), as well as models with variable star formation efficiency (SFE; left panel) and radial flows (right panel). Note that the absolute Nitrogen abundance values in the Palla et al. (2020) models were divided by a factor of 2.6 to match our observations.

for Nitrogen in the Milky Way. In both panels of Figure 11 we show a model that includes inside-out growth only (dark grey), which shows a shallower distribution compared with observations, suggesting that this mechanism alone is insufficient to reproduce the observed Nitrogen abundance gradient. In the left panel Figure 11 we show models with variable star formation efficiency labeled B, F, and G, and the right panel of Figure 11 we show models with radial flows labeled C, D, and E in Palla et al. (2020). We refer to Palla et al. (2020) for specific parameters assumed for these models. As we can see, in agreement with the conclusion in Palla et al. (2020), the variable SFE model F, and the radial flow model E, agree the best with the observed Nitrogen abundance gradients. Thus, in a addition to inside-out growth, variable SFE and/or radial flows are necessary to explain the observed of the Nitrogen abundance gradient for $R_{\text{gal}} > 4$ kpc.

Note that absolute value of the predicted Nitrogen abundances in the Palla et al. (2020) models are on average a factor of 2.6 (0.41 dex) larger than the observed values. In Figure 11 we adjusted the model predicted absolute Nitrogen abundances by this factor so that their average value coincides with the Nitrogen abundance predicted by the fit in Equation (16) at 4 kpc. The Palla et al. (2020) models assume stellar yields for massive stars from Kobayashi et al. (2006, 2011), and for low-intermediate mass stars from Karakas (2010), and uncertainties in stellar yield calculations might result in an overestimation in the production of Nitrogen. In addition, based on optical spectroscopy of stars that show the presence two, higher and lower metallicity, populations of

massive stars in the disk of the Milky Way, it has been recently hypothesized that a recent accretion episode (in addition to the two-infall model) of low metallicity gas in the Milky Way disk in the last 2.7 Gyr have resulted in a general ISM metal impoverishment (Spitoni et al. 2023, Palla et al. 2024 in prep.). Given that the Nitrogen abundances derived here those by Arellano-Córdova et al. (2021) trace the recent production of Nitrogen in the Milky way, our observations would be consistent with this hypothesis.

In Figure 9, we see a peak in the N/H abundance at $R_{\text{gal}} \simeq 4$ kpc, which is associated with the outermost part of the Galactic Bar (Benjamin et al. 2005). A bar potential can efficiently redistribute angular momentum and mass in galaxies, and the radial flows produced by such a potential are expected to mix elemental abundances, flattening any abundance gradient over time (Friedli & Benz 1993; Friedli et al. 1994). The star formation rate in the Milky Way peaks at $R_{\text{gal}} \approx 4$ kpc, and do not continue to rise for smaller Galactocentric radii (Pineda et al. 2014; Elia et al. 2022). Therefore the formation of new elements in the inner 4 kpc must be less efficient. Note that the observed reduction in the star formation rate in the inner Galaxy is likely due to a reduction of the number of star forming regions per unit area compared with larger Galactocentric distances.

Chemical evolution models predict elemental abundances to reach an equilibrium value in regions where the production of new elements is balanced by metal consumption by star formation and expulsion by outflows (Peng & Maiolino 2014; Weinberg et al. 2017). The time scales for reaching the

Table 7. Derived Nitrogen Abundances in the Galactic Plane for $l \geq 0^\circ$

LOS	l	b	n_e	T_e	$N(\text{N}^+)$	$N(\text{H}^+)$	$12+\log(\text{N}^+/\text{H}^+)$	R_{gal}
	[$^\circ$]	[$^\circ$]	[cm^{-3}]	[K]	[10^{17}cm^{-2}]	[10^{20}cm^{-2}]		[kpc]
G000.0+0.0	0.000	0.0	121.5 ± 0.5	11910 ± 97	35.8 ± 0.12	50.6 ± 0.9	7.8 ± 0.0	0.0 ± 0.0
G000.5+0.0	0.500	0.0	40.9 ± 23.4	12855 ± 706	9.9 ± 3.17	49.7 ± 19.3	7.3 ± 0.1	0.1 ± 0.0
G003.5+0.0	3.478	0.0	16.3 ± 0.3	5421 ± 1340	3.9 ± 0.04	2.4 ± 1.1	8.2 ± 0.2	5.2 ± 0.0
G004.3+0.0	4.348	0.0	24.7 ± 0.8	7791 ± 3330	2.2 ± 0.04	1.6 ± 1.4	8.1 ± 0.4	5.2 ± 0.0
G005.2+0.0	5.217	0.0	6.6 ± 0.5	7513 ± 1844	11.7 ± 0.29	7.6 ± 3.8	8.2 ± 0.2	5.2 ± 0.0
G006.1+0.0	6.087	0.0	18.8 ± 7.2	6969 ± 1992	5.3 ± 1.21	4.2 ± 1.5	8.1 ± 0.2	0.9 ± 0.0
G007.8+0.0	7.826	0.0	27.5 ± 0.5	10043 ± 1644	3.4 ± 0.03	4.5 ± 1.5	7.9 ± 0.1	6.0 ± 1.4
G008.7+0.0	8.696	0.0	14.3 ± 0.8	12852 ± 3316	11.1 ± 0.25	21.7 ± 12.0	7.7 ± 0.2	5.5 ± 0.0
G010.4+0.0	10.435	0.0	24.3 ± 0.5	6129 ± 367	10.1 ± 0.13	12.3 ± 1.5	7.9 ± 0.1	1.5 ± 0.0
G011.3+0.0	11.304	0.0	8.3 ± 0.6	4556 ± 707	10.5 ± 0.31	6.8 ± 2.2	8.2 ± 0.1	5.7 ± 0.0
G012.2+0.0	12.174	0.0	23.4 ± 0.4	5800 ± 648	10.9 ± 0.12	5.4 ± 1.2	8.3 ± 0.1	4.5 ± 0.0
G013.0+0.0	13.043	0.0	29.6 ± 0.4	7647 ± 1046	3.8 ± 0.03	5.1 ± 1.4	7.9 ± 0.1	5.7 ± 1.2
G013.9+0.0	13.913	0.0	17.9 ± 0.6	3501 ± 170	7.2 ± 0.15	9.4 ± 0.9	7.9 ± 0.0	4.7 ± 0.0
G014.8+0.0	14.783	0.0	21.6 ± 0.7	10169 ± 1904	7.2 ± 0.13	6.3 ± 2.5	8.1 ± 0.2	4.8 ± 0.0
G016.5+0.0	16.522	0.0	25.9 ± 0.2	5716 ± 1301	4.5 ± 0.02	3.4 ± 1.6	8.1 ± 0.2	5.2 ± 0.6
G020.0+0.0	20.000	0.0	12.5 ± 0.2	6479 ± 1706	4.7 ± 0.03	6.9 ± 3.8	7.8 ± 0.2	3.9 ± 0.6
G020.9+0.0	20.870	0.0	25.0 ± 0.7	6335 ± 566	6.5 ± 0.11	7.2 ± 1.3	8.0 ± 0.1	4.5 ± 0.0
G021.7+0.0	21.739	0.0	29.2 ± 0.7	12850 ± 1891	9.2 ± 0.13	6.9 ± 2.2	8.1 ± 0.1	6.3 ± 0.0
G023.5+0.0	23.478	0.0	26.0 ± 0.2	5949 ± 339	17.7 ± 0.11	12.1 ± 1.4	8.2 ± 0.1	4.1 ± 0.0
G024.3+0.0	24.348	0.0	18.1 ± 0.3	5744 ± 276	14.5 ± 0.13	11.3 ± 1.1	8.1 ± 0.0	3.8 ± 0.3
G025.2+0.0	25.217	0.0	12.8 ± 0.4	9093 ± 3292	14.9 ± 0.18	11.9 ± 9.2	8.1 ± 0.3	4.4 ± 0.6
G026.1+0.0	26.087	0.0	38.8 ± 0.4	5630 ± 198	14.9 ± 0.12	7.8 ± 0.5	8.3 ± 0.0	3.9 ± 0.0
G027.0+0.0	26.956	0.0	22.0 ± 0.3	10085 ± 1915	6.7 ± 0.04	6.6 ± 2.7	8.0 ± 0.2	4.1 ± 0.0
G028.7+0.0	28.696	0.0	37.6 ± 0.6	8663 ± 612	10.6 ± 0.11	10.9 ± 1.6	8.0 ± 0.1	4.0 ± 0.0
G030.0+0.0	30.000	0.0	31.8 ± 0.9	13227 ± 2184	8.6 ± 0.14	11.5 ± 4.0	7.9 ± 0.2	4.1 ± 0.0
G031.3+0.0	31.277	0.0	25.8 ± 0.4	5548 ± 170	12.1 ± 0.12	11.7 ± 0.7	8.0 ± 0.0	4.8 ± 0.6
G036.4+0.0	36.383	0.0	20.8 ± 1.7	7445 ± 1652	3.3 ± 0.16	3.2 ± 1.5	8.0 ± 0.2	5.6 ± 0.0
G037.7+0.0	37.660	0.0	17.1 ± 0.5	5299 ± 214	9.6 ± 0.16	9.8 ± 0.8	8.0 ± 0.0	5.5 ± 0.2
G041.5+0.0	41.489	0.0	46.8 ± 0.5	10619 ± 1481	2.2 ± 0.02	2.8 ± 0.8	7.9 ± 0.1	7.3 ± 0.0
G044.0+0.0	44.043	0.0	13.8 ± 0.3	4308 ± 929	3.4 ± 0.05	3.4 ± 1.5	8.0 ± 0.2	6.5 ± 0.6
G045.3+0.0	45.319	0.0	29.3 ± 1.1	6955 ± 1313	0.9 ± 0.02	1.8 ± 0.7	7.7 ± 0.2	6.1 ± 0.0
G049.1+0.0	49.149	0.0	21.7 ± 1.7	13245 ± 2858	3.3 ± 0.13	6.5 ± 3.0	7.7 ± 0.2	6.2 ± 0.0
G054.3+0.0	54.255	0.0	46.0 ± 1.0	10888 ± 2869	1.1 ± 0.02	1.6 ± 0.9	7.8 ± 0.2	6.6 ± 0.0

equilibrium abundance are different for each element, with elements such as Oxygen and Nitrogen reaching their equilibrium at the timescale at which gas is being depleted by star formation and outflows, while Fe reaches equilibrium at this timescale or that of SNe Ia enrichment (~ 1.5 Gyr), whichever is longer (Weinberg et al. 2017). Belfiore et al. (2017) observed a flattening of the O/H abundance in the center of galaxies with stellar masses similar to that of the Milky Way, but observed that the O/N ratio continues to rise toward the center of these galaxies. They interpreted this result as Oxygen reaching an equilibrium abundance, but Nitrogen is continuously being produced by secondary nucleosynthetic production, in longer-living, intermediate mass stars. We do not observe this effect in the center of the Milky Way, suggesting that the timescales for a Nitrogen abundance equi-

librium has not been reached in the inner Milky Way. Note however, that the star formation rate in the Milky Way peaks at $R_{\text{gal}} = 4$ kpc (Pineda et al. 2014; Elia et al. 2022), and thus the high star formation rate required for the equilibrium hypothesis is not reached at smaller radii. We therefore favor radial flows induced by the stellar bar as the most likely mechanism for the flattening of the Nitrogen abundance in the innermost parts of the Galaxy.

4. SUMMARY

We presented a Galactic plane survey of Hydrogen Radio Recombination Lines (RRLs) observed with the NASA DSS-43 70m antenna and the Green Bank Telescope. We observed 108 lines-of-sights covering a range between $-135^\circ < l < 60^\circ$ and $b = 0^\circ$ in the Galactic plane. We

Table 8. Derived Nitrogen Abundances in the Galactic Plane for $l < 0^\circ$

LOS	l	b	n_e	T_e	$N(\text{N}^+)$	$N(\text{H}^+)$	$12+\log(\text{N}^+/\text{H}^+)$	R_{gal}
	[$^\circ$]	[$^\circ$]	[cm^{-3}]	[K]	[10^{17}cm^{-2}]	[10^{20}cm^{-2}]		[kpc]
G302.6+0.0	302.553	0.0	12.5 ± 0.2	4015 ± 481	5.3 ± 0.04	7.9 ± 2.0	7.8 ± 0.1	7.1 ± 0.0
G305.1+0.0	305.106	0.0	4.9 ± 0.2	4321 ± 162	31.5 ± 0.34	55.9 ± 4.9	7.8 ± 0.0	7.0 ± 0.0
G306.4+0.0	306.383	0.0	9.9 ± 0.4	8090 ± 1043	3.9 ± 0.06	7.8 ± 2.2	7.7 ± 0.1	6.6 ± 0.0
G307.7+0.0	307.660	0.0	15.4 ± 0.9	8658 ± 309	5.9 ± 0.17	8.7 ± 0.9	7.8 ± 0.0	6.5 ± 0.0
G310.2+0.0	310.213	0.0	62.3 ± 2.1	8792 ± 539	0.6 ± 0.02	1.9 ± 0.3	7.5 ± 0.1	7.4 ± 1.1
G314.0+0.0	314.043	0.0	26.4 ± 0.3	8349 ± 706	2.5 ± 0.02	4.6 ± 0.8	7.7 ± 0.1	6.2 ± 0.0
G316.6+0.0	316.596	0.0	21.0 ± 0.6	8844 ± 372	9.8 ± 0.16	14.5 ± 1.4	7.8 ± 0.0	7.0 ± 0.8
G317.9+0.0	317.872	0.0	25.3 ± 0.9	9234 ± 477	5.9 ± 0.12	11.9 ± 1.4	7.7 ± 0.1	8.0 ± 1.4
G326.8+0.0	326.808	0.0	26.5 ± 0.4	5199 ± 317	11.2 ± 0.12	9.0 ± 1.2	8.1 ± 0.1	5.8 ± 0.0
G330.0+0.0	330.000	0.0	39.0 ± 1.0	13446 ± 6062	1.6 ± 0.02	4.2 ± 4.1	7.6 ± 0.4	5.2 ± 0.5
G331.7+0.0	331.739	0.0	29.5 ± 1.0	16634 ± 4501	7.6 ± 0.14	9.2 ± 5.3	7.9 ± 0.2	5.7 ± 0.0
G332.6+0.0	332.609	0.0	25.6 ± 0.9	3941 ± 571	4.8 ± 0.11	6.5 ± 2.0	7.9 ± 0.1	5.1 ± 0.6
G333.5+0.0	333.478	0.0	36.8 ± 0.6	7703 ± 991	8.7 ± 0.09	8.8 ± 2.4	8.0 ± 0.1	5.3 ± 0.6
G336.1+0.0	336.087	0.0	28.5 ± 0.3	8161 ± 1282	18.5 ± 0.11	14.3 ± 4.7	8.1 ± 0.1	3.9 ± 0.6
G337.0+0.0	336.957	0.0	31.9 ± 0.3	15478 ± 2066	23.0 ± 0.14	32.6 ± 9.0	7.8 ± 0.1	3.8 ± 0.6
G337.8+0.0	337.826	0.0	22.6 ± 10.8	14731 ± 5334	16.7 ± 5.64	13.3 ± 6.2	8.1 ± 0.2	3.1 ± 0.0
G338.7+0.0	338.696	0.0	28.0 ± 0.3	6405 ± 906	3.8 ± 0.03	6.2 ± 1.8	7.8 ± 0.1	5.4 ± 0.0
G342.2+0.0	342.174	0.0	11.0 ± 0.6	8643 ± 1176	11.5 ± 1.98	15.1 ± 2.9	7.9 ± 0.1	3.0 ± 0.0
G343.9+0.0	343.913	0.0	21.7 ± 11.1	16864 ± 5699	4.3 ± 2.09	3.6 ± 2.3	8.1 ± 0.2	3.0 ± 0.0
G345.7+0.0	345.652	0.0	25.2 ± 10.2	15869 ± 6014	10.5 ± 2.68	21.7 ± 12.5	7.7 ± 0.3	2.0 ± 0.0
G346.5+0.0	346.522	0.0	30.4 ± 1.5	8642 ± 1394	3.4 ± 0.11	7.5 ± 2.6	7.7 ± 0.1	5.6 ± 1.3
G349.1+0.0	349.130	0.0	52.2 ± 0.5	5674 ± 207	13.1 ± 0.09	19.7 ± 1.3	7.8 ± 0.0	2.8 ± 0.0
G350.9+0.0	350.870	0.0	14.4 ± 1.3	5845 ± 1572	3.1 ± 0.14	6.5 ± 3.8	7.7 ± 0.2	4.4 ± 0.0
G353.5+0.0	353.478	0.0	17.0 ± 5.1	12417 ± 3271	7.0 ± 1.61	6.9 ± 2.2	8.0 ± 0.1	3.4 ± 0.0
G354.3+0.0	354.348	0.0	31.8 ± 2.1	8488 ± 1212	2.7 ± 0.11	4.0 ± 1.2	7.8 ± 0.1	2.9 ± 0.0
G355.2+0.0	355.217	0.0	87.8 ± 3.0	12528 ± 1706	2.7 ± 0.07	4.7 ± 1.2	7.8 ± 0.1	4.2 ± 0.0
G356.1+0.0	356.087	0.0	35.3 ± 0.3	10465 ± 2529	2.8 ± 0.01	3.1 ± 1.5	8.0 ± 0.2	4.2 ± 0.0
G359.5+0.0	359.500	0.0	47.3 ± 21.4	20202 ± 2209	13.5 ± 3.96	19.9 ± 6.2	7.8 ± 0.1	0.1 ± 0.0

combined these observations with observations of the [N II] $122\mu\text{m}$ and $205\mu\text{m}$ lines taken with the *Herschel* space observatory and [N III] $57\mu\text{m}$ taken with SOFIA/FIFI-LS, and radio continuum data, to characterize the distribution of the Nitrogen abundance across the disk of the Milky Way. In a sample of 41 LOS, where we have high enough signal-to-noise ratio, we studied the distribution of the ionized Nitrogen abundance relative to ionized Hydrogen covering galactocentric distances between 0 to 8 kpc. Combined with existing determinations of the N/H abundance in the solar neighborhood and outer Galaxy, we are able to study for the first time the distribution of this quantity in the inner 16 kpc of the Milky Way. The results of this work can be summarized as follows:

- We find a Nitrogen abundance gradient extending over Galactocentric distances between 4 and 17 kpc in the Galactic plane, while for 0 to 4 kpc we find a flat N/H distribution.
- The gradient observed at Galactocentric distances larger than 4 kpc supports inside-out galaxy growth with the additional steepening resulting from variable star formation efficiency and/or radial flows in the Galactic disk.
- The observed flattening of the Nitrogen abundance distribution in the inner 4 kpc, which coincides with the start of the Galactic bar, can be associated with radial flows induced by the bar potential.
- We studied the ionization structure of a sub-sample of 8 LOS for which we obtained [N III] $57\mu\text{m}$ observations, and [O III] $88\mu\text{m}$ and $52\mu\text{m}$ observations in Sagittarius A. We find that most of the Nitrogen in our sample is likely singly ionized, which is consistent with their locations being in low ionization outskirts of H II regions, and that any highly ionized Nitrogen comes from compact high electron density H II regions.

Our observations demonstrate the power of using of far-infrared spectral lines and radio recombination lines, for an unobscured study of the ionization structure and the Nitrogen abundance distribution in galaxies. Far-infrared observatories, such as the GUSTO and ASTHROS balloons, and a future NASA far-infrared probe mission, together with ground based radio observatories, such as e.g. the GBT and NASA DSN antennas, can provide important insights in the chemical evolution in galaxies, which in turn provide important information to models of galaxy evolution.

This research was carried out at the Jet Propulsion Laboratory, California Institute of Technology, under a contract with the National Aeronautics and Space Administration. The work in this publication was supported by NASA’s Astrophysics Data Analysis Program (ADAP) under grant No. 80NM0018F0610,18-2ADAP18-0196. We would like to acknowledge and express our gratitude to Javier Goicoechea for kindly providing the *Herschel*/PACS data in Sagittarius A. We also extend our sincere appreciation to Karla Arellano-Cordova for contributing the optical Nitrogen abundance data and to Marco Palla for supplying the model Nitrogen abundance distributions and for their insightful discus-

sions. Their inputs and contributions have greatly enriched and strengthened our work. We also thank the anonymous referee for comments that significantly improved the paper. This project made use of the Smithsonian Astrophysical Observatory $4 \times 32\text{k}$ -channel spectrometer (SAO32k) and the *TAMS observatoryCtrl* observing system, which were developed by L. Greenhill (Center for Astrophysics), I. Zaw (New York University Abu Dhabi), D. Price, and D. Shaff, with funding from SAO and the NYUAD Research Enhancement Fund and in-kind support from the Xilinx University Program. We thank West Virginia University for its financial support of GBT operations, which enabled the observations for this project. The National Radio Astronomy Observatory is a facility of the National Science Foundation operated under cooperative agreement by Associated Universities, Inc. LDA and ML are supported by NSF grant AST1516021 to LDA. We thank the staff of the SOFIA Science Center for their help. U.S. Government sponsorship acknowledged.

Software: TMBIDL (Bania et al. 2014), GILDAS/CLASS (Pety 2005)

Facilities: GBT, DSN/DSS–43, SOFIA, Herschel

APPENDIX

A. DEPENDENCE OF NITROGEN ABUNDANCE DISTRIBUTION ON ELECTRON TEMPERATURES DERIVED FROM DIFFERENT RADIO CONTINUUM SURVEYS.

In Figure 12 we show the N^+/H^+ distribution as a function of Galactocentric distance derived using electron temperatures derived from each of the radio continuum surveys listed in Table 5. In general, most LOS with $l < 0^\circ$ are covered by the SGPS and/or the Parkes 6 cm survey. For sources with $l \geq 0^\circ$, all sources are covered by either the Effelsberg/GLOSTAR survey at 4.88 GHz and 6.82 GHz and the Nobeyama 10.3 GHz survey. A subsample is also covered by the VGPS survey at 1.4 GHz. Each panel in Figure 12 are labeled with the combination of surveys used to cover the entire range of Galactic longitudes. Note that some LOS do not appear in all panels because they do not meet the $\text{SNR} > 10$ criteria for the free-free brightness temperature. We also show the N^+/H^+ distribution resulting from using the averaged free-free continuum temperature as described in Section 3.1.1. We find that N^+/H^+ distribution is not significantly affected by the choice of radio continuum survey used to derive electron temperatures.

B. COMPARISON WITH BALSER ET AL. 2015 ELECTRON TEMPERATURES.

The uncertainties derived for the electron temperatures described in Section 3.1.1 are based on the uncertainties of the measurements of the continuum and RRL emission, and therefore do not account for calibration uncertainties, that can vary for the different frequency spectral bands used for the continuum emission, and the accuracy of our correction for synchrotron emission. To assess the sensitivity of the derived electron temperatures to these uncertainties we compared our methodology to derive electron temperatures against electron temperatures derived in a sample of H II regions by Balser et al. (2015) in which calibration uncertainties and synchrotron contribution are carefully assessed.

Balser et al. (2015) derived electron temperatures in a sample of 21 H II regions in the Galactic plane in both RRL and continuum emission at 8.7 GHz using the Green Bank Telescope. This sample was selected to have a continuum intensity signal-to-noise ratio greater than 10 and to be isolated enough so that spatial and spectral blending can be avoided. Because the RRL and continuum observations are done in the same band, with the same telescope, these measurements do not suffer from calibration uncertainties. Also, because the spatial structure in continuum is well isolated, the free-free and synchrotron emission can be separated by fitting the compact free-free emission with a Gaussian function and the more extended synchrotron emission with a low order polynomial baseline. Therefore a comparison between the electron temperatures derived by Balser et al. (2015) and those derived using our methodology can be used to assess the impact of calibration uncertainties and free-free/synchrotron separation in the electron temperatures derived in our sample.

There are however a few differences between our sources and those used by Balser et al. (2015). Their sources are compact H II regions, while our sources are associated with the outskirts of H II regions. As discussed in Section 3.1.1, the beam filling effects in our Galactic plane sample are small but are more significant for the Balser et al. (2015) sample. Also, the electron densities

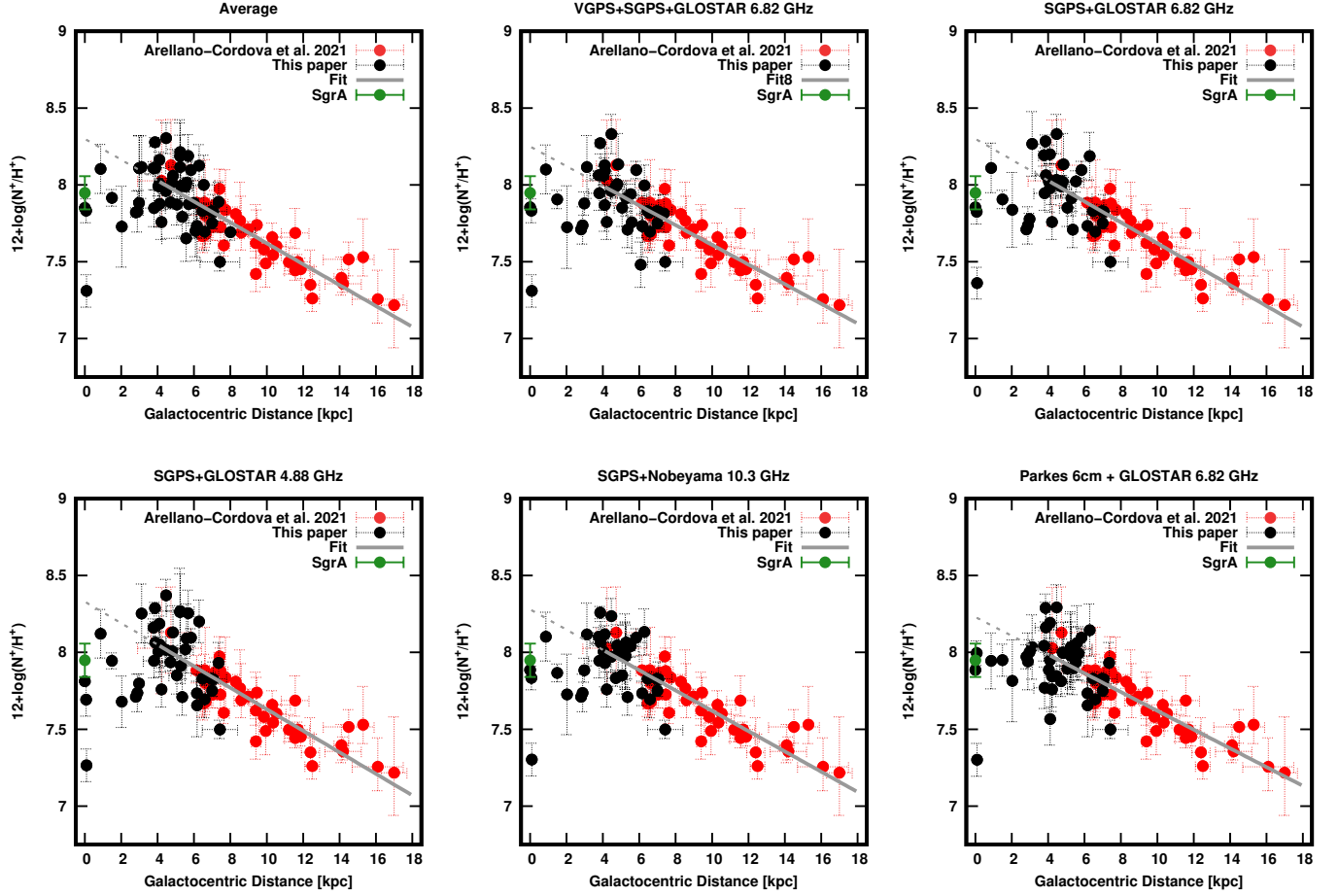


Figure 12. The fractional abundance of ionized Nitrogen with respect to ionized Hydrogen as a function of Galactocentric distance derived for different combinations of radio continuum surveys. Note that the different surveys listed cover the majority of sources with $R_{\text{gal}} > 5$ kpc.

in this sample are likely to be larger than the typical densities in our sample. For this comparison, we will not apply a non-LTE correction, as we did for our sample.

In the left panel of Figure 13, we show a comparison between the electron temperatures derived from RRL and continuum intensities from [Balsler et al. \(2015\)](#) and those derived using our methodology with the RRL intensities from [Balsler et al. \(2015\)](#) but with the continuum intensities extracted from the Effelsberg 100 m GLOSTAR data at 6.82 GHz. The angular resolution of the Effelsberg data set is $106''$ which is somewhat larger than the $87''$ resolution of the GBT data. We find good agreement between the electron temperatures using the two methods. The scatter from the one-to-one correlation between the electron temperatures derived from these two methods is on average 18%. This difference can arise from the different angular resolution of the data, which can be important due to the compact H II emission in this sample, from the uncertainties in the relative calibration between the Effelsberg and GBT data sets, and/or from the separation between free-free and synchrotron emission, with the latter estimated to be on average 19% of the total continuum emission at 6.82 GHz.

To better test our prediction for the contribution from synchrotron emission in our method, we use 1.4 GHz data, where synchrotron emission is expected to be more significant. We derive electron temperatures using the VLA Galactic plane survey data set, which covers the Galactic latitude range of the [Balsler et al. \(2015\)](#) sample. This comparison helped us to assess our derivation of electron temperatures in sources in the southern hemisphere, where we used the SGPS data set at 1.4 GHz. We convolved the $60''$ resolution VGPS survey to $87''$ to match the angular resolution of the GBT data set. In the right panel of Figure 13 we show a comparison between the electron temperatures derived using our method against those derived from the [Balsler et al. \(2015\)](#) data set. We find that electron temperatures have a similar range with scatter around the one-to-one correlation. In this case, the difference between electron temperatures derived using our method and those from [Balsler et al. \(2015\)](#) is on average 33%. As before, these differences can arise from uncertainties in the relative calibrations between the VGPS and GBT data sets and/or from the separation between free-free and synchrotron emission, which is on average 38% of the continuum emission at 1.4 GHz in this sample.

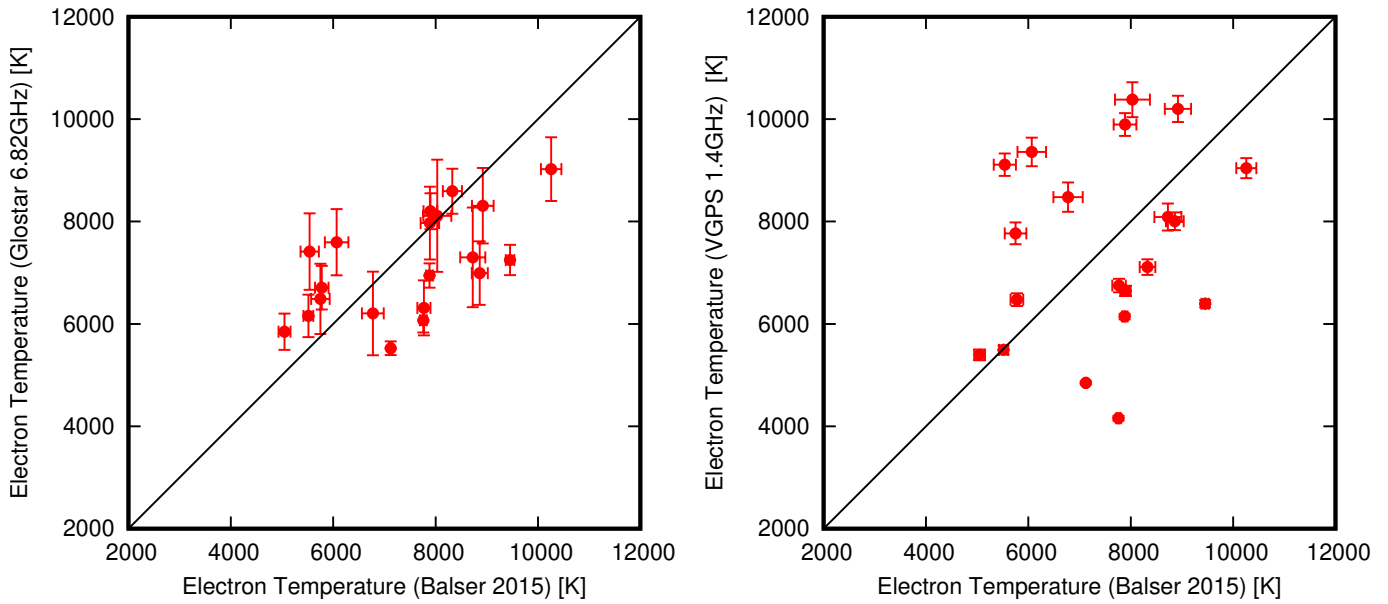


Figure 13. (*left*) Comparison between electron temperatures derived by Balser et al. (2015) using Green Bank Telescope and those derived with the same RRL emission but with continuum intensities derived from the GLOSTAR/Effelsberg 6.82 GHz radio continuum survey. (*right*) Comparison between electron temperatures derived by Balser et al. (2015) using Green Bank Telescope and those derived with the same RRL emission but with continuum intensities derived from the VGPS 1.4 GHz radio continuum survey.

In summary, a comparison between our method to derive electron temperatures using 1.4 GHz and 6.82 GHz observations shows that additional uncertainties between 20% to 30% can arise due to uncertainties in the calibration of several continuum bands and in our correction for the contribution of synchrotron emission. Note that these uncertainties are reduced by using a combination of several radio continuum data sets in the derivation of electron temperatures as discussed in Section 3.1.1.

REFERENCES

- Afflerbach, A., Churchwell, E., & Werner, M. W. 1997, *ApJ*, 478, 190, doi: [10.1086/303771](https://doi.org/10.1086/303771)
- Akhmetov, V. S., Bucciarelli, B., Crosta, M., et al. 2024, *MNRAS*, 530, 710, doi: [10.1093/mnras/stae772](https://doi.org/10.1093/mnras/stae772)
- Akritas, M. G., & Bershad, M. A. 1996, *ApJ*, 470, 706, doi: [10.1086/177901](https://doi.org/10.1086/177901)
- Anderson, L. D., Bania, T. M., Balser, D. S., et al. 2014, *ApJS*, 212, 1, doi: [10.1088/0067-0049/212/1/1](https://doi.org/10.1088/0067-0049/212/1/1)
- Anderson, L. D., Bania, T. M., Balser, D. S., & Rood, R. T. 2011, *ApJS*, 194, 32, doi: [10.1088/0067-0049/194/2/32](https://doi.org/10.1088/0067-0049/194/2/32)
- Andrievsky, S. M., Martin, R. P., Kovtyukh, V. V., Korotin, S. A., & Lépine, J. R. D. 2016, *MNRAS*, 461, 4256, doi: [10.1093/mnras/stw1631](https://doi.org/10.1093/mnras/stw1631)
- Arellano-Córdova, K. Z., Esteban, C., García-Rojas, J., & Méndez-Delgado, J. E. 2021, *MNRAS*, 502, 225, doi: [10.1093/mnras/staa3903](https://doi.org/10.1093/mnras/staa3903)
- Balser, D. S. 2006, *AJ*, 132, 2326, doi: [10.1086/508515](https://doi.org/10.1086/508515)
- Balser, D. S., Rood, R. T., Bania, T. M., & Anderson, L. D. 2011, *ApJ*, 738, 27, doi: [10.1088/0004-637X/738/1/27](https://doi.org/10.1088/0004-637X/738/1/27)
- Balser, D. S., Wenger, T. V., Anderson, L. D., & Bania, T. M. 2015, *ApJ*, 806, 199, doi: [10.1088/0004-637X/806/2/199](https://doi.org/10.1088/0004-637X/806/2/199)
- Bania, T., Wenger, T., Balser, D., & Anderson, L. 2014, Tmbidl V8.0, Zenodo Software Release, 2014, doi: [10.5281/zenodo.32790](https://doi.org/10.5281/zenodo.32790)
- . 2016, TMBIDL: Single dish radio astronomy data reduction package, Astrophysics Source Code Library, doi: [10.5281/zenodo.32790](https://doi.org/10.5281/zenodo.32790)
- Bania, T. M., Anderson, L. D., Balser, D. S., & Rood, R. T. 2010, *ApJL*, 718, L106, doi: [10.1088/2041-8205/718/2/L106](https://doi.org/10.1088/2041-8205/718/2/L106)
- Belfiore, F., Maiolino, R., Tremonti, C., et al. 2017, *MNRAS*, 469, 151, doi: [10.1093/mnras/stx789](https://doi.org/10.1093/mnras/stx789)
- Benjamin, R. A., Churchwell, E., Babler, B. L., et al. 2005, *ApJL*, 630, L149, doi: [10.1086/491785](https://doi.org/10.1086/491785)
- Boissier, S., & Prantzos, N. 1999, *MNRAS*, 307, 857, doi: [10.1046/j.1365-8711.1999.02699.x](https://doi.org/10.1046/j.1365-8711.1999.02699.x)
- Brocklehurst, M., & Seaton, M. J. 1972, *MNRAS*, 157, 179, doi: [10.1093/mnras/157.2.179](https://doi.org/10.1093/mnras/157.2.179)
- Brunthaler, A., Menten, K. M., Dzib, S. A., et al. 2021, *A&A*, 651, A85, doi: [10.1051/0004-6361/202039856](https://doi.org/10.1051/0004-6361/202039856)
- Calabrò, A., Daddi, E., Cassata, P., et al. 2018, *ApJL*, 862, L22, doi: [10.3847/2041-8213/aad33e](https://doi.org/10.3847/2041-8213/aad33e)

- Chiappini, C., Matteucci, F., & Gratton, R. 1997, *ApJ*, 477, 765, doi: [10.1086/303726](https://doi.org/10.1086/303726)
- Davies, B., Origlia, L., Kudritzki, R.-P., et al. 2009, *ApJ*, 696, 2014, doi: [10.1088/0004-637X/696/2/2014](https://doi.org/10.1088/0004-637X/696/2/2014)
- Elia, D., Molinari, S., Schisano, E., et al. 2022, *ApJ*, 941, 162, doi: [10.3847/1538-4357/aca27d](https://doi.org/10.3847/1538-4357/aca27d)
- Esteban, C., & García-Rojas, J. 2018, *MNRAS*, 478, 2315, doi: [10.1093/mnras/sty1168](https://doi.org/10.1093/mnras/sty1168)
- Fadda, D., & Chambers, E. T. 2018, in *American Astronomical Society Meeting Abstracts*, Vol. 231, American Astronomical Society Meeting Abstracts #231, 150.11
- Fischer, C., Beckmann, S., Bryant, A., et al. 2018, *Journal of Astronomical Instrumentation*, 1840003, doi: [10.1142/s2251171718400032](https://doi.org/10.1142/s2251171718400032)
- Friedli, D., & Benz, W. 1993, *A&A*, 268, 65
- Friedli, D., Benz, W., & Kennicutt, R. 1994, *ApJL*, 430, L105, doi: [10.1086/187449](https://doi.org/10.1086/187449)
- Goicoechea, J. R., Etxaluze, M., Cernicharo, J., et al. 2013, *ApJL*, 769, L13, doi: [10.1088/2041-8205/769/1/L13](https://doi.org/10.1088/2041-8205/769/1/L13)
- Goldsmith, P. F., Yıldız, U. A., Langer, W. D., & Pineda, J. L. 2015, *ApJ*, 814, 133, doi: [10.1088/0004-637X/814/2/133](https://doi.org/10.1088/0004-637X/814/2/133)
- Gordon, M. A., & Sorochenko, R. L., eds. 2002, *Astrophysics and Space Science Library*, Vol. 282, *Radio Recombination Lines. Their Physics and Astronomical Applications*. <http://adsabs.harvard.edu/abs/2002ASSL..282.....G>
- Grisoni, V., Matteucci, F., & Romano, D. 2021, *MNRAS*, 508, 719, doi: [10.1093/mnras/stab2579](https://doi.org/10.1093/mnras/stab2579)
- Handa, T., Sofue, Y., Nakai, N., Hirabayashi, H., & Inoue, M. 1987, *PASJ*, 39, 709
- Haslam, C. G. T., Klein, U., Salter, C. J., et al. 1981, *A&A*, 100, 209
- Haverkorn, M., Gaensler, B. M., McClure-Griffiths, N. M., Dickey, J. M., & Green, A. J. 2006, *ApJS*, 167, 230, doi: [10.1086/508467](https://doi.org/10.1086/508467)
- Hayden, M. R., Holtzman, J. A., Bovy, J., et al. 2014, *AJ*, 147, 116, doi: [10.1088/0004-6256/147/5/116](https://doi.org/10.1088/0004-6256/147/5/116)
- Haynes, R. F., Caswell, J. L., & Simons, L. W. J. 1978, *Australian Journal of Physics Astrophysical Supplement*, 45, 1
- Johnson, J. A. 2019, *Science*, 363, 474, doi: [10.1126/science.aau9540](https://doi.org/10.1126/science.aau9540)
- Karakas, A. I. 2010, *MNRAS*, 403, 1413, doi: [10.1111/j.1365-2966.2009.16198.x](https://doi.org/10.1111/j.1365-2966.2009.16198.x)
- Kobayashi, C., Karakas, A. I., & Umeda, H. 2011, *MNRAS*, 414, 3231, doi: [10.1111/j.1365-2966.2011.18621.x](https://doi.org/10.1111/j.1365-2966.2011.18621.x)
- Kobayashi, C., Umeda, H., Nomoto, K., Tominaga, N., & Ohkubo, T. 2006, *ApJ*, 653, 1145, doi: [10.1086/508914](https://doi.org/10.1086/508914)
- Kubryk, M., Prantzos, N., & Athanassoula, E. 2015, *A&A*, 580, A127, doi: [10.1051/0004-6361/201424599](https://doi.org/10.1051/0004-6361/201424599)
- Langer, W. D., & Pineda, J. L. 2015, *A&A*, 580, A5, doi: [10.1051/0004-6361/201525950](https://doi.org/10.1051/0004-6361/201525950)
- Langer, W. D., Velusamy, T., Pineda, J. L., et al. 2010, *A&A*, 521, L17, doi: [10.1051/0004-6361/201015088](https://doi.org/10.1051/0004-6361/201015088)
- Langer, W. D., Pineda, J. L., Goldsmith, P. F., et al. 2021, *A&A*, 651, A59, doi: [10.1051/0004-6361/202040223](https://doi.org/10.1051/0004-6361/202040223)
- LaRosa, T. N., Kassim, N. E., Lazio, T. J. W., & Hyman, S. D. 2000, *AJ*, 119, 207, doi: [10.1086/301168](https://doi.org/10.1086/301168)
- Larson, R. B. 1976, *MNRAS*, 176, 31, doi: [10.1093/mnras/176.1.31](https://doi.org/10.1093/mnras/176.1.31)
- Luisi, M., Anderson, L. D., Liu, B., Anish Roshni, D., & Churchwell, E. 2019, *ApJS*, 241, 2, doi: [10.3847/1538-4365/aaf6a5](https://doi.org/10.3847/1538-4365/aaf6a5)
- Maiolino, R., & Mannucci, F. 2019, *A&A Rv*, 27, 3, doi: [10.1007/s00159-018-0112-2](https://doi.org/10.1007/s00159-018-0112-2)
- Martin, R. P., Andrievsky, S. M., Kovtyukh, V. V., et al. 2015, *MNRAS*, 449, 4071, doi: [10.1093/mnras/stv590](https://doi.org/10.1093/mnras/stv590)
- Matteucci, F. 2021, *A&A Rv*, 29, 5, doi: [10.1007/s00159-021-00133-8](https://doi.org/10.1007/s00159-021-00133-8)
- Matteucci, F., & Francois, P. 1989, *MNRAS*, 239, 885, doi: [10.1093/mnras/239.3.885](https://doi.org/10.1093/mnras/239.3.885)
- Medina, S. N. X., Urquhart, J. S., Dzib, S. A., et al. 2019, *A&A*, 627, A175, doi: [10.1051/0004-6361/201935249](https://doi.org/10.1051/0004-6361/201935249)
- Mizutani, M., Onaka, T., & Shibai, H. 2002, *A&A*, 382, 610, doi: [10.1051/0004-6361:20011611](https://doi.org/10.1051/0004-6361:20011611)
- Najarro, F., Figer, D. F., Hillier, D. J., Geballe, T. R., & Kudritzki, R. P. 2009, *ApJ*, 691, 1816, doi: [10.1088/0004-637X/691/2/1816](https://doi.org/10.1088/0004-637X/691/2/1816)
- Palla, M., Matteucci, F., Spitoni, E., Vincenzo, F., & Grisoni, V. 2020, *MNRAS*, 498, 1710, doi: [10.1093/mnras/staa2437](https://doi.org/10.1093/mnras/staa2437)
- Peng, Y.-j., & Maiolino, R. 2014, *MNRAS*, 443, 3643, doi: [10.1093/mnras/stu1288](https://doi.org/10.1093/mnras/stu1288)
- Pérez-Montero, E., García-Benito, R., Vílchez, J. M., et al. 2016, *A&A*, 595, A62, doi: [10.1051/0004-6361/201628601](https://doi.org/10.1051/0004-6361/201628601)
- Persic, M., Salucci, P., & Stel, F. 1996, *MNRAS*, 281, 27, doi: [10.1093/mnras/281.1.27](https://doi.org/10.1093/mnras/281.1.27)
- Pety, J. 2005, in *SF2A-2005: Semaine de l'Astrophysique Française*, ed. F. Casoli, T. Contini, J. M. Hameury, & L. Pagani, 721
- Pezzulli, G., & Fraternali, F. 2016, *MNRAS*, 455, 2308, doi: [10.1093/mnras/stv2397](https://doi.org/10.1093/mnras/stv2397)
- Pilkington, K., Few, C. G., Gibson, B. K., et al. 2012, *A&A*, 540, A56, doi: [10.1051/0004-6361/201117466](https://doi.org/10.1051/0004-6361/201117466)
- Pineda, J. L., Langer, W. D., & Goldsmith, P. F. 2014, *A&A*, 570, A121, doi: [10.1051/0004-6361/201424054](https://doi.org/10.1051/0004-6361/201424054)
- Pineda, J. L., Langer, W. D., Velusamy, T., & Goldsmith, P. F. 2013, *A&A*, 554, A103, doi: [10.1051/0004-6361/201321188](https://doi.org/10.1051/0004-6361/201321188)
- Pineda, J. L., Horiuchi, S., Anderson, L. D., et al. 2019, *ApJ*, 886, 1, doi: [10.3847/1538-4357/ab46c2](https://doi.org/10.3847/1538-4357/ab46c2)
- Puglisi, A., Daddi, E., Renzini, A., et al. 2017, *ApJL*, 838, L18, doi: [10.3847/2041-8213/aa66c9](https://doi.org/10.3847/2041-8213/aa66c9)
- Quiroza, C., Rood, R. T., Balser, D. S., & Bania, T. M. 2006, *ApJS*, 165, 338, doi: [10.1086/503901](https://doi.org/10.1086/503901)

- Reid, M. J., Dame, T. M., Menten, K. M., & Brunthaler, A. 2016, *ApJ*, 823, 77, doi: [10.3847/0004-637X/823/2/77](https://doi.org/10.3847/0004-637X/823/2/77)
- Reid, M. J., Menten, K. M., Brunthaler, A., et al. 2014, *ApJ*, 783, 130, doi: [10.1088/0004-637X/783/2/130](https://doi.org/10.1088/0004-637X/783/2/130)
- . 2019, *ApJ*, 885, 131, doi: [10.3847/1538-4357/ab4a11](https://doi.org/10.3847/1538-4357/ab4a11)
- Rohlfs, K., & Wilson, T. L. 2004, *Tools of radio astronomy (Tools of radio astronomy, 4th rev. and enl. ed., by K. Rohlfs and T.L. Wilson. Berlin: Springer, 2004)*
- Romano, D. 2022, *A&A Rv*, 30, 7, doi: [10.1007/s00159-022-00144-z](https://doi.org/10.1007/s00159-022-00144-z)
- Romano, D., Karakas, A. I., Tosi, M., & Matteucci, F. 2010, *A&A*, 522, A32, doi: [10.1051/0004-6361/201014483](https://doi.org/10.1051/0004-6361/201014483)
- Rudolph, A. L., Fich, M., Bell, G. R., et al. 2006, *ApJS*, 162, 346, doi: [10.1086/498869](https://doi.org/10.1086/498869)
- Rudolph, A. L., Simpson, J. P., Haas, M. R., Erickson, E. F., & Fich, M. 1997, *ApJ*, 489, 94, doi: [10.1086/304758](https://doi.org/10.1086/304758)
- Sánchez, S. F., Rosales-Ortega, F. F., Iglesias-Páramo, J., et al. 2014, *A&A*, 563, A49, doi: [10.1051/0004-6361/201322343](https://doi.org/10.1051/0004-6361/201322343)
- Sánchez-Menguiano, L., Sánchez, S. F., Pérez, I., et al. 2016, *A&A*, 587, A70, doi: [10.1051/0004-6361/201527450](https://doi.org/10.1051/0004-6361/201527450)
- Simpson, J. P., Colgan, S. W. J., Rubin, R. H., Erickson, E. F., & Haas, M. R. 1995, *ApJ*, 444, 721, doi: [10.1086/175645](https://doi.org/10.1086/175645)
- Simpson, J. P., Rubin, R. H., Colgan, S. W. J., Erickson, E. F., & Haas, M. R. 2004, *ApJ*, 611, 338, doi: [10.1086/422028](https://doi.org/10.1086/422028)
- Sormani, M. C., Treß, R. G., Glover, S. C. O., et al. 2019, *MNRAS*, 488, 4663, doi: [10.1093/mnras/stz2054](https://doi.org/10.1093/mnras/stz2054)
- Spitoni, E., Recio-Blanco, A., de Laverny, P., et al. 2023, *A&A*, 670, A109, doi: [10.1051/0004-6361/202244349](https://doi.org/10.1051/0004-6361/202244349)
- Steiman-Cameron, T. Y., Wolfire, M., & Hollenbach, D. 2010, *ApJ*, 722, 1460, doi: [10.1088/0004-637X/722/2/1460](https://doi.org/10.1088/0004-637X/722/2/1460)
- Stil, J. M., Taylor, A. R., Dickey, J. M., et al. 2006, *AJ*, 132, 1158, doi: [10.1086/505940](https://doi.org/10.1086/505940)
- Virkler, K., Kocz, J., Soriano, M., et al. 2020, *ApJS*, 251, 1, doi: [10.3847/1538-4365/abbace](https://doi.org/10.3847/1538-4365/abbace)
- Weinberg, D. H., Andrews, B. H., & Freudenburg, J. 2017, *ApJ*, 837, 183, doi: [10.3847/1538-4357/837/2/183](https://doi.org/10.3847/1538-4357/837/2/183)
- Wenger, T. V., Balsa, D. S., Anderson, L. D., & Bania, T. M. 2018, *ApJ*, 856, 52, doi: [10.3847/1538-4357/aaec8](https://doi.org/10.3847/1538-4357/aaec8)
- Wenger, T. V., Dickey, J. M., Jordan, C. H., et al. 2019, *ApJS*, 240, 24, doi: [10.3847/1538-4365/aaf8ba](https://doi.org/10.3847/1538-4365/aaf8ba)
- Wong, G. F., Horiuchi, S., Green, J. A., et al. 2016, *MNRAS*, 458, 151, doi: [10.1093/mnras/stw004](https://doi.org/10.1093/mnras/stw004)
- Zhou, Y., Li, X., Huang, Y., & Zhang, H. 2023, *ApJ*, 946, 73, doi: [10.3847/1538-4357/acadd9](https://doi.org/10.3847/1538-4357/acadd9)